Martian polar and circum-polar sulfate-bearing deposits: Sublimation tills derived from the north polar cap

Marion Massé, Olivier Bourgeois, Stéphane Le Mouélic, Charles Verpoorter, Laetitia Le Deit, Jean-Pierre Bibring

Accepted Manuscript

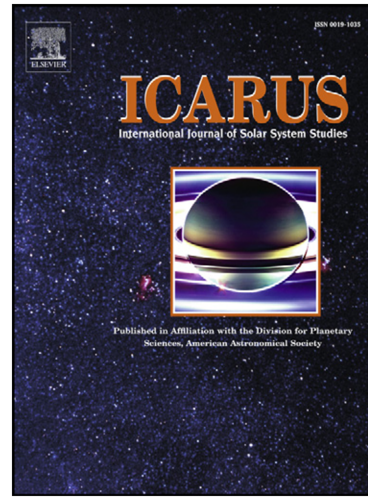

Martian polar and circum-polar sulfate-bearing deposits: Sublimation tills derived from the north polar cap

M. Massé, O. Bourgeois, S. Le Mouélic, C. Verpoorter, L. Le Deit, J.P. Bibring

PII: S0019-1035(10)00174-0
DOI: 10.1016/j.icarus.2010.04.017
Reference: YICAR 9414

To appear in: *Icarus*

Received Date: 22 January 2010
Revised Date: 21 April 2010
Accepted Date: 21 April 2010

Please cite this article as: Massé, M., Bourgeois, O., Le Mouélic, S., Verpoorter, C., Le Deit, L., Bibring, J.P., Martian polar and circum-polar sulfate-bearing deposits: Sublimation tills derived from the north polar cap, *Icarus* (2010), doi: 10.1016/j.icarus.2010.04.017

MARTIAN POLAR AND CIRCUM-POLAR SULFATE-BEARING DEPOSITS: SUBLIMATION TILLS DERIVED FROM THE NORTH POLAR CAP

M. Massé[a], O. Bourgeois[a], S. Le Mouélic[a], C. Verpoorter[a,b], L. Le Deit[a,c] and J.P. Bibring[d]

[a] *Laboratoire de Planétologie et Géodynamique, UMR 6112, CNRS, Université de Nantes, 2 chemin de la Houssinière, BP 92205, 44322 Nantes Cedex 3,(France).*

marion.masse@univ-nantes.fr

olivier.bourgeois@univ-nantes.fr

stephane.lemouelic@univ-nantes.fr

[b] *Laboratoire d'Océanologie et de Géosciences, UMR LOG 8187, 32 avenue Foch, 62930 Wimereux, (France).*

Charles.Verpoorter@univ-littoral.fr

[c] *Institute of Planetary Research, German Aerospace Center (DLR), Rutherfordstr.2, 12489 Berlin, (Germany).*

Laetitia.LeDeit@dlr.de

[d] *Institut d'Astrophysique Spatiale, Universite´ Paris XI, Orsay, (France).*

jean-pierre.bibring@ias.u-psud.fr

Number of pages: 48

Number of figures: 13

Proposed Running Head:

Origin of Martian circum-polar gypsum bearing deposits

Please send Editorial Correspondence to:

Marion Massé
Laboratoire de Planétologie et Géodynamique,
UMR 6112, CNRS, Université de Nantes,
2 chemin de la Houssinière, BP 92205,
44322 Nantes Cedex 3, France

Email: marion.masse@univ-nantes.fr
Phone: +(0)332.51.12.54.67

Abstract

Previous spectroscopic studies have shown the presence of hydrated minerals in various kinds of sedimentary accumulations covering and encircling the Martian North Polar Cap. More specifically, gypsum, a hydrated calcium sulfate, has been detected on Olympia Planum, a restricted part of the Circumpolar Dune Field. To further constrain the geographical distribution and the process of formation and accumulation of these hydrated minerals, we performed an integrated morphological, structural and compositional analysis of a key area where hydrated minerals were detected and where the main polar landforms are present. By the development of a spectral processing method based on spectral derivation and by the acquisition of laboratory spectra of gypsum-ice mixtures we find that gypsum-bearing sediment is not restricted to the Olympia Planum dunes but is also present in all kinds of superficial sediment covering the surface of the North Polar Cap and the Circumpolar Dune Field. Spectral signatures consistent with perchlorates are also detected on these deposits. The interpretation of landforms reveals that this gypsum-bearing sediment was released from the ice cap by sublimation. We thus infer that gypsum crystals that are now present in the Circum-Polar Dune Field derive from the interior of the North Polar Cap. Gypsum crystals that were initially trapped in the ice cap have been released by sublimation of the ice and have accumulated in the form of ablation tills at the surface of the ice cap. These gypsum-bearing sublimation tills are reworked by winds and are transported towards the Circum-Polar Dune Field. Comparison with sulfates found in terrestrial glaciers suggests that gypsum crystals in the Martian North Polar Cap have formed by weathering of dust particles, either in the atmosphere prior to their deposition during the formation of the ice cap, and/or in the ice cap after their deposition.

Keywords: Mars, polar caps; Mars, polar geology; mineralogy; Ices, IR Spectroscopy; Mars, surface.

1. Introduction

Various kinds of sulfates have been discovered in several regions of Mars, both from in-situ ground observations by the Spirit and Opportunity rovers and from orbital observations by the OMEGA and CRISM imaging spectrometers. In equatorial and mid-latitude regions, Mg-, Fe- and Ca-sulfates have been detected in light toned layered deposits and in soils [e.g. Christensen et al., 2004; Gendrin et al., 2005; Arvidson et al., 2006; Squyres et al., 2006; Le Deit et al., 2008, Massé et al., 2008; Roach et al., 2009; Wray et al., 2009]. At higher latitudes, Ca-sulfates have been detected in dark dune fields in the vicinity of the North Polar Cap [Langevin et al., 2005b; Roach et al., 2007] and possibly in the permafrost of the Phoenix landing site [Hecht et al., 2009]. Understanding the origin of these various kinds of sulfate-bearing deposits is of importance because they constitute key elements to constrain the evolution of the Martian surface and past climate. Various hypotheses have been suggested so far to explain their formation. On Earth, large accumulations of sulfates commonly form in evaporitic environments [Rouchy and Blanc-Valleron, 2006]; one of the classical hypotheses for the formation of sulfates on Mars is therefore evaporitic concentration and deposition in water bodies [Catling, 1999]. Other classical hypotheses involve in-situ weathering of sulphide deposits or basaltic materials by acid fogs or acid groundwaters [see review in Chevrier and Mathé, 2007]. Recently, Niles and Michalski [2009] suggested that Martian equatorial sulfates have formed by weathering of dust trapped in ancient equatorial ice caps. Figure 1

Interestingly, the largest accumulation of sulfates detected so far on Mars is located on Olympia Planum, a crescent-shaped dome, 500 km in radius, located at the present-day border of the North Polar Cap (Fig. 1a and b) [Langevin et al., 2005b; Roach et al., 2007]. This dome corresponds to an ancient part of the North Polar Cap, which has been exhumed by erosional retreat of its upper part [Zuber et al., 1998; Fishbaugh and Head, 2000, 2005]. This dome is now extensively covered by superficial sediment and dark dunes. These correspond to the densest part of the Circum-Polar Dune Field that encircles the whole North Polar Cap [Fishbaugh et al., 2007; Tanaka and Hayward, 2008]. The spectral signature of hydrated Ca-sulfate (most likely gypsum) observed by OMEGA and CRISM in this region is correlated to the dark dunes that cover Olympia Planum (Fig. 1b) [Langevin et al., 2005b; Roach et al., 2007].

The presence of gypsum in dunes resting on an erosional relict of the North Polar Cap raises the question of whether a link exists between the processes of formation and/or accumulation of these circum-polar sulfates and the past or present activity of the ice cap. The aim of our study is therefore to evaluate, by an integrated morphological, structural and compositional analysis, whether polar and circum-polar gypsum-rich deposits, such as those observed in Olympia Planum, derive from the North Polar Cap or not. Figure 2

For that purpose, we focus on a key area located at the border of the North Polar Cap, between Olympia Cavi and Gemini Scopuli (Fig. 1a and 2). This area provides a comprehensive view, on the same location, of (1) the Circum-Polar Dune Field, (2) the surface of the North Polar Cap and (3) a natural cross-section that reveals the internal structure of the ice cap. Morphological and structural information on this area is provided by the analysis of HiRISE and CTX images and MOLA topographic data, while compositional constraints are provided by the analysis of CRISM and OMEGA hyperspectral data.

In section 2, we briefly describe the North Polar Cap, the associated polar and circum-polar superficial accumulations of dark sediment (including the Circum-Polar Dune Field) and we review current hypotheses for the origin of the circum-polar sulfate deposits. Then, we introduce in section 3 the structure and landforms of the study area and discuss their significance. In section 4, we present the results of the spectroscopic compositional analysis. We finally discuss in section 5 the implications for the origin of polar and circumpolar sulfates.

2. Geological setting

2.1 The North Polar Cap

The North Polar Cap rests in the lowest part of the Vastistas Borealis topographic basin (Fig. 1a and c). It is 1300 km in diameter and reaches a maximum thickness of 3 km at its center [Zuber et al., 1998]. The formation of the whole ice cap took place during the Amazonian [Carr and Head, 2009]. It is a stack of water ice layers containing various amounts of intermixed sediment (dust or sand) [Kieffer et al., 1976; Tsoar at al., 1979; Howard et al., 1982; Fishbaugh et al., 2008]. Two distinct units have been recognized in this stack (Fig. 1c). The first one corresponds to the Basal Unit (BU), which rests directly on the Vastistas Borealis Formation (VBF). High-resolution images reveal that the BU consists of a low albedo, 1 km-thick formation displaying platy interbedded sequences of ice-rich and sediment-rich layers [Byrne and Murray, 2002; Edgett et al., 2003; Fishbaugh and Head, 2005]. SHARAD and MARSIS radar soundings have confirmed the existence of this sediment-rich BU, and have revealed that it is largely confined to the major lobe of the North Polar Cap (Fig. 1) [Picardi et al., 2005; Phillips et al., 2008; Putzig et al., 2009]. The second unit corresponds to the upper (and younger) part of the ice cap, which is composed of the North Polar Layered Deposits (NPLD). On high-resolution images, the NPLD appear brighter and more finely layered than the BU. The majority of the NPLD is made of water ice and their layering results from varying fractions of included sediment and/or varying ice grain sizes [Kiefer et al., 1976; Calvin et al., 2009]. Radar soundings have confirmed that the amount of sediment in the NPLD is small, with only ~2% for most layers and ~30% for a few strong radar reflective layers [Picardi et al., 2005; Phillips et al., 2008]. On the basis of morphological and sedimentary interpretation of high-resolution images, Tanaka et al. [2008] subdivided the BU and the NPLD into a full suite of stratigraphic units.

The surface morphology of the North Polar Cap is dominated by interior spiral troughs and marginal steep arcuate scarps [Howard, 2000] (Fig. 1a and c). These spiral troughs and arcuate scarps provide natural cross-sections where the internal structure of the North Polar Cap can be observed. Spiral troughs only cut through the NPLD and do not reach the BU [Putzig et al., 2009]. The most widely accepted hypothesis for their formation is ablation due to katabatic winds and sublimation [Howard, 2000; Ivanov and Muhleman, 2000]. Katabatic winds and sublimation are most probably also responsible for the formation of the marginal arcuate scarps [Warner and Farmer, 2008]. The correlation between the location of the arcuate scarps and the spatial extent of the BU has been attributed to preferential undermining of the scarp bases because of the presence of sand in the BU [Howard, 2000; Edgett et al., 2003].

During Martian winters, a layer of CO_2 and H_2O frost, approximately one meter in thickness, covers the North Polar Cap. This seasonal frost coverage begins to sublimate in spring and has disappeared by the end of summer [Smith et al., 2001b; Byrne et al., 2008].

2.2 Polar and circum-polar superficial accumulations of dark sediment

In addition to sediment intermixed in the ice of the BU and of the NPLD, dark polar and circum-polar sediment has also been observed in the form of (1) superficial accumulations on the floors of some spiral troughs, (2) extensive superficial mantles (classically named dark veneers [Rodriguez et al., 2007]) covering the surface of the NPLD, and (3) dunes located in the Circum-Polar Dune Field [Rodriguez et al., 2007; Horgan et al., 2009]. The sources of the dark veneers and of the sedimentary accumulations in spiral troughs are sediment-rich layers of the NPLD [Rodriguez et al., 2007; Tanaka et al., 2008].

The Circum-Polar Dune Field is the largest dune field on Mars. It extends between 70°N and 85°N in latitude and entirely rings the North Polar Cap (Fig. 1b). Most of the dark dunes constituting the Circum-Polar Dune Field have been classified as transverse and barchan dunes [Tsoar et al., 1979]. Based on the shape of these dunes and on their systematic association with arcuate scarps, Thomas and Weitz [1989] inferred that the source of the circum-polar dune material is sand that was initially contained within the North Polar Cap. Herkenhoff and Vasada [1999] thus conjectured that the dune material might be composed of filamentary sublimation residue formed by concentration of dust in sand-size aggregates during sublimation of the ice cap. Alternatively, it has been suggested that the major source for the circum-polar dune material is sand derived from the BU rather than dust derived from the whole ice cap [Fishbaugh and Head, 2005; Herkenhoff et al., 2007].

2.3 Sulfates in polar and circum-polar superficial sediment

Spectroscopic studies have revealed unambiguous signatures of a calcium-rich hydrated sulfate (most likely gypsum) on Olympia Planum (Fig. 1b) [Langevin et al., 2005b, Roach et al., 2007]. In this portion of the Circum-Polar Dune Field, the density of dunes is at its highest [Tanaka and Hayward, 2008]. In the inter-dune substrate of Olympia Planum, Roach et al. [2007] detected gypsum signatures, which appear weaker than those found on dunes. These weak signatures indicate either that small amounts of fine-grained gypsum are present within the bulk of the inter-dune substrate or that a thin layer of gypsum-rich particles covers the inter-dune substrate.

Poulet et al. [2005], Horgan et al. [2009] and Calvin et al. [2009] detected spectroscopic signatures of hydrated minerals on the entire Circum-Polar Dune Field, on the NPLD dark veneers and on the sedimentary accumulations covering spiral troughs. It is unclear however whether these signatures correspond to gypsum, to another kind of hydrated sulfate or more generally to any other hydrated minerals. If these signatures do correspond to gypsum, as they do in Olympia Planum, their weakness has to be attributed either (1) to low gypsum concentrations, (2) to scattering effects due to texture, or (3) to spatial exposures of gypsum being too small to be resolved with the spatial resolution of the instrument [Calvin et al., 2009].

The darkness of the circum-polar sediments suggests that they are not pure gypsum. Poulet et al. [2005] and Horgan and Bell [2009] have also identified signatures of mafic minerals, which could explain their low albedo. Alternatively, Fishbaugh et al. [2007] suggested that secondary oxides may darken these sediments.

2.4 Currently proposed origins for circum-polar sulfates

Because of its softness, gypsum is easily susceptible to physical weathering; therefore the gypsum detected on Olympia Planum has probably formed in-situ or within a short distance from its current location [Fishbaugh et al., 2007]. On this basis, Langevin et al. [2005b] suggested two different hypotheses for the formation of gypsum in Olympia Planum: interaction of Ca-rich minerals with snow containing H_2SO_4 derived from volcanic activity or formation as an evaporite deposit after major meltwater outflows from the ice cap during warm climatic incursions. Fishbaugh et al. [2007] suggested that water from nearby channels percolated through dunes that cover the eastern end of Olympia Planum and attributed the formation of gypsum there to a combination of (1) in-situ aqueous weathering of sulfide- and high-calcium-pyroxene-bearing dune materials and (2) formation of evaporitic gypsum crystals in the pore spaces of these materials. Szynkiewicz et al. [2010] suggested that gypsum crystals were formed by evaporation of saline waters and were later transported by winds towards Olympia Planum.

Alternatively, it has been suggested that gypsum minerals could derive directly from the underlying BU [Roach et al., 2007; Calvin et al., 2009]; this interpretation would be consistent with the possible existence of small amounts of gypsum in the inter-dune substrate [Roach et al., 2007].

To further constrain the extent and the origin of polar and circum-polar sulfate deposits, we focus on a key area which encompasses all the features described above (Fig. 2): (1) the surface of the North Polar Cap, (2) two spiral troughs, (3) two marginal arcuate scarps providing natural cross-sections through the NPLD and the BU and (4) a portion of the Circum-Polar Dune Field. This area is located at the border of the North Polar Cap, between Olympia Cavi and Gemini Scopuli, at the latitude of 83°N and the longitude of 118°E. The portion of the Circum-Polar Dune Field comprised in this study area is located outside the gypsum-rich area previously identified by Langevin et al. [2005b] (Fig. 1b), but spectroscopic signatures of hydrated minerals have been detected there [Horgan et al., 2009; Calvin et al., 2009]. Based on a detailed morphological and compositional analysis of this area, we will demonstrate that gypsum is present in all kinds of polar and circum-polar superficial accumulations of dark sediment, and that it derives from the ice cap.

3. Structure and landforms of the study area

3.1. Data and Methods

We investigate the structure and landforms of the study area with complementary data sets, which provide different kinds of information. All these datasets have been incorporated into a geographic information system using the Mars 2000 geographic coordinate system and the polar stereographic projection.

Topographic information is provided by the Mars Orbiter Laser Altimeter (MOLA). The selected polar digital terrain model has a relative vertical accuracy of 1 m and an average spatial resolution of 512 pixel / degree [Smith et al., 2001a]. Geomorphological and structural information is provided by (1) images of the Context Camera (CTX) with a spatial resolution of 6 m/pixel over a swath that is about 30 km wide [Malin et al., 2007], (2) images of the High Resolution Imaging Science Experiment (HiRISE) with a resolution up to 30 cm/pixel for a swath width of 6 km [McEwen et al., 2007]. Since we aim at observing sediment in the bulk and at the surface of the permanent ice cap, we use CTX and HiRISE images acquired in summer only, in order to minimize the effect of the seasonal CO_2 and H_2O frost coverage.

3.2. Description of landforms in the study area

A CTX image, an interpretative sketch-map and an interpretative cross-section of the whole study area are shown in Fig. 3. Figure 3

The surface of the NPLD occupies the northern half of the image. The outer reaches of two spiral troughs strike NW-SE across the NPLD (Fig. 2 and 3). In the area encompassed by the image, these troughs are 300 to 500 m deep. Unlike other spiral troughs observed elsewhere on the North Polar Cap by Rodriguez et al. [2007] and Horgan et al. [2009], the troughs of the study area are not covered by dark sediment. The internal layering of the NPLD is thus exposed in these troughs. Differences in albedo between the exposed layers indicate either that they contain differing amounts of sediment intermixed with the ice or that they have differing ice grain sizes [Calvin et al., 2009]. Along the northern border of the northernmost trough, the surface of a dissected packet of ice layers forms a tabular outcrop covered by dark sediment and bordered by an escarpment 100 m-high (Fig. 3).

In the central-eastern and south-western parts of the image, two arcuate scarps, facing south, cut through the NPLD (Fig. 2 and 3). The northernmost arcuate scarp is ~25 km wide and extends beyond the eastern border of the image; its maximal height is 500 m. The southernmost one is ~20 km wide and extends beyond the western border of the image; its maximal height is 300 m.

The average slope gradient is 30° in the steepest parts of both scarps. The two arcuate scarps intersect, hence were probably carved later than, the spiral troughs.

These scarps provide vertical sections through the whole stack of NPLD present in this area, and the BU that has been exhumed at their base (Fig. 3). The BU is distinguishable from the NPLD by a break in topographic slope at the base of the scarps (Fig. 3c and d), by its darker tone due to its larger concentration in sediment, and by the fact that the beds of the BU form resistant shelves, and are organized in platy interbedded sequences of ice-rich and sediment-rich layers (Fig. 3c). The fact that the BU crops out at the base of arcuate scarps in this region is consistent with the extension of the BU as inferred from radar soundings [Putzig et al., 2009] (Fig. 1 and 2).

South of each scarp, the topographic surface dips gently northwards. In these latter regions, superficial sediment and dunes of the Circum-Polar Dune Field cover the NPLD and the BU, except for the southernmost part of the image where ice is visible (Fig. 3).

3.3. Release of dark superficial sediment towards dune fields by horizontal ablation of ice layers at arcuate scarps

On Earth, the formation of steep arcuate marginal scarps is typical of those glaciers where sublimation is the dominant process of ablation. These include equatorial glaciers such as those located on the Kilimanjaro in Africa and polar glaciers such as those located in the Dry Valleys in Antarctica. It has been shown that these steep terrestrial ice walls are erosional forms that move backward by horizontal regressive ablation of the ice under the effect of radiant heating [Fountain et al., 2006; Hoffman et al., 2008; Mölg and Hardy, 2004; Mölg et al., 2003, 2008]. We infer that the steep arcuate scarps observed in the study area have formed by a similar process of horizontal regressive ablation of the North Polar Cap. In the pressure and temperature conditions currently prevailing at these latitudes on Mars, sublimation is the most probable process by which ablation of ice and erosional retreat of the scarps may have occurred [Ivanov and Muhleman, 2000].

The substrate of the regions lying at the bottom of the two arcuate scarps comprises the BU and the NPLD (Fig. 3a, b, d). This substrate is covered by a superficial mantle of dark sediment and by dark dune fields. These are separated from the corresponding scarps by distances of 0 to 6 km (Fig. 3a and b). The dunes belong to the barchan or barchanoid types defined by McKee [1979] and Hayward et al. [2007], which are indicative of unidirectional winds [Bagnold, 1954]. The orientation of the dunes indicates that the dominant wind blows down scarp from the NE (Fig. 3a and b).

The northern border of each dune field comprises a belt of large barchans, which is particularly well defined for the northernmost field (Fig. 3a and b). The presence of this upwind belt is classical in terrestrial dune fields and can be explained by the fact that dunes of the first row lose less sand than they gain and turn into mega dunes [Bagnold, 1954; Tsoar et al, 1979]. At a distance of 0 to 900 m from their upwind border belts, both dune fields are constituted by smaller, closely packed, barchanoids. At the down-wind portions of the fields, the end barchans have a tendency to disperse. This organization is consistent with the wind blowing dominantly from the NE down the surface of the North Polar Cap and down the scarps. Frost streaks at the surface of the NPLD also indicate that the wind blows dominantly from the NE (Fig. 3a).

At the feet of both scarps, dark streamers striking NE are visible (Fig. 3a and c). These features indicate that dark sediment that has been released from ice layers ablated by the retreat of the scarps was accumulated at their feet in the form of dark sublimation tills covering the NPLD and the BU. This sediment is then transported by the wind towards the dune fields.

All of our observations in this region are thus consistent with the systematic association, elsewhere around the North Polar Cap, of dune fields with arcuate scarps and with the corresponding interpretation that the material present in the Circum-Polar Dune Field derives from the North Polar Cap [Tsoar et al., 1979; Thomas and Weitz, 1989; Howard, 2000; Warner and Farmer, 2008]. We infer that this material (1) was released from the ice cap as the arcuate scarps retreated by sublimation, (2) was then mobilized by katabatic winds descending along the surface of the North Polar Cap and (3) was eventually deposited in dune fields around the ice cap.

3.4. Release of dark sediment at the surface of the NPLD by vertical ablation of ice layers

Figure 4

The northern (south-facing) slope of the northernmost spiral trough is interrupted by an escarpment 100 m high (Fig. 3). We interpret this scalloped escarpment as the erosional front of a dissected packet of ice layers (Fig. 4a and d). Above the escarpment is a 3 km wide topographic plateau entirely covered by dark sediment and corresponding to an erosional surface that developed at the expense of this packet of ice layers. Erosional remnants of the uppermost layers of the packet appear in the form of linear tongues and ovoid tabular ridges striking East-West, a few hundred meters in average width, that are entirely covered by dark sediment (Fig. 4a, b and d). At the center of some of these ovoid ridges is a depression where the superficial dark sediment is less abundant (Fig. 4a and b). These remnant buttes indicate that some ice layers, which formerly covered the whole plateau, have now been extensively dissected by erosion. Sublimation is the major process by which near complete ablation of these layers can have occurred in this region [Ivanov and Muhleman, 2000]. This interpretation is supported by the existence of similar landforms in terrestrial glaciers subjected to sublimation, such as on the Kilimanjaro [Mölg and Hardy, 2004; Mölg et al., 2003, 2008].

Between the remnant buttes, the plateau has a specific roughness, composed of closely spaced, regular, polygonal hollows (Fig. 4b). These hollows are 20 to 50 m in diameter and are separated from each other by ridges that form a "honeycomb-like network" [Milkovich and Head, 2006]. Differences in albedo between the hollow centers and the boundary ridges reveal that the sediment is denser on the ridges than in the hollows. This specific kind of surface texture is common on terrestrial glaciers and snowfields (Fig. 4c). It is known as ablation hollows or suncups [Rhodes et al., 1987; Betterton, 2001]. Terrestrial ablation hollows form through radiant heating of the ice surface due to direct or indirect sunlight, which causes ablation of the ice by melting or sublimation [Rhodes et al., 1987; Betterton, 2001; Milkovich and Head, 2006]. These features grow because hollow centers receive more reflected light than ridges. As surface lowering by ablation proceeds, any sediment particle that was initially present within the bulk of the ice will move in a trajectory perpendicular to the surface and the sediment will thus concentrate on the ridges [Rhodes et al, 1987]. Though they have not unambiguously observed them, Milkovich and Head [2006] postulated that ablation hollows likely exist on the North Polar Cap of Mars. On Earth, these features generally form by surface melting. By contrast, under the pressure and temperature conditions prevailing at these latitudes on Mars, the development of ablation hollows most probably involves sublimation [Ivanov and Muhleman, 2000; Milkovich and Head, 2006]. The difference in size between terrestrial ablation hollows (typically 0.1 – 1 m in diameter) and those described here (20 – 50 m) is attributable to either (1) differences in initial sediment concentration within the ice, (2) differences in conditions of radiant heating, (3) differences in the process of ablation (melting on Earth versus sublimation on Mars) or (4) differences in the time available for their development (one season at most on Earth versus several years at least on Mars). The effect of each these various parameters on the size of ablation hollows is poorly known because of the lack of measurements and physical models on their development. Betterton (2001) however demonstrated that the amount of sediment strongly controls the size of suncups and it seems reasonable to assume that longer development times will help create larger features.

Our observations on this dissected plateau thus demonstrate the presence of a superficial accumulation of sediment on an ablation surface that developed at the expense of a packet of ice layers. The concentration of this superficial sediment on ridges forming a honeycomb-like network is best explained by a process, well known on terrestrial glaciers, according to which the sediment that was initially present within the bulk of the ice has concentrated at the surface by vertical ablation of the ice.

This interpretation is supported by the fact that this superficial accumulation of sediment can be traced from place to place, along the same sub-horizontal ice layers, throughout the study area (Fig. 3a, b and d). Had this sediment been imported from elsewhere and had it been deposited unconformably from above after the formation of the ablation surface, its extent would not fit that of the ice layers. We thus infer that the superficial sediment covering the plateau has been released from the eroding packet of ice layers itself (Fig. 3d); it has concentrated in the form of a sublimation till on the surface of the ice cap, as ablation by sublimation dissected this sediment-rich packet of ice layers.

3.5. Synthesis: origin of polar and circum-polar accumulations of dark sediment

We have shown that in the region under study, dune fields are fed by sediment released from arcuate scarps that develop by regressive ablation of the North Polar Cap. This sediment may derive either from the BU exhumed at the base of the arcuate scarps or from the NPLD that covered the area before erosional retreat of the arcuate scarps. We have also shown evidence that sediment accumulations at the surface of the NPLD are released by vertical ablation of sediment-rich ice layers of the NPLD.

As a conclusion, the superficial sediment present on the NPLD and in the Circum-Polar Dune Field derives from the North Polar Cap. This sediment, which was initially intermixed within the bulk of the ice, now forms ablation tills that have concentrated at the ice surface by sublimation. Katabatic winds are responsible for its re-mobilization and its deposition in the Circum-Polar Dune Field. Previous observations elsewhere on the North Polar Cap are consistent with this interpretation [Tsoar et al., 1979; Thomas and Weitz, 1989; Herkenhoff and Vasada, 1999;

Howard, 2000; Fishbaugh and Head, 2005; Rodriguez et al., 2007; Tanaka et al., 2008; Warner and Farmer, 2008].

4. Mineralogical analysis

Two different hypotheses remain for the origin of gypsum crystals that have been observed in Olympia Planum and that are possibly present in the Circum-Polar Dune Field as a whole. Similarly to the dark sediment described in part 3, gypsum crystals may have been initially present within the bulk of the ice of the North Polar Cap, may have been released to the surface by ablation, and transported towards dunes [Calvin et al., 2009]. Alternatively, they may have formed as secondary minerals in dunes, at the expense or in the pore spaces of the dark sediment derived from the North Polar Cap [Langevin et al., 2005b; Fishbaugh et al., 2007]. To evaluate the validity of the first hypothesis, we must be able to detect the presence of gypsum in the North Polar Cap from orbital hyperspectral data. For that purpose, we have first investigated the spectral behavior of experimental ice-gypsum mixtures in Martian pressure and temperature conditions. The results of this laboratory study were then used to derive the composition of sediments associated with the North Polar Cap from the available orbital hyperspectral data.

4.1. Spectral behavior of experimental ice-gypsum mixtures

4.1.1. Experimental procedure

In order to investigate the spectral behavior of ice-gypsum mixtures, we have acquired laboratory reflectance spectra of ice samples containing various volumetric proportions of gypsum. The ice was produced by condensation of liquid water on a cooled metal plate [Dupire et al., 2009]. It was then crushed to obtain grain sizes between 500 and 600 µm. These ice grains were homogenously mixed with an industrial pure gypsum powder (producer: Merck Chemicals; reference: 102160, commercial name: calcium sulfate dihydrate precipitated, chemical formula:

$CaSO_4 * 2H_2O$, grain size: less than 10µm). The samples were then placed in a liquid nitrogen cryostat (MicrostatN, Oxford Instruments) to reproduce the Martian pressure and temperature conditions (7 mbar, 150 K) and their spectra were acquired with a Nicolet 5700 Fourier Transform Infrared Spectrometer, which collects 4149 spectral channels from 1 to 5 µm.

4.1.2. Results

Figure 5

Fig. 5 displays the laboratory spectra obtained for pure water ice, pure gypsum, a mixture composed of ~50% ice and ~50% gypsum in volume and a mixture composed of ~30% ice and ~70% gypsum in volume. Pure water ice displays specific absorption bands at 1.04 µm and 1.25 µm, two broad absorption bands between 1.50 and 1.66 µm and between 1.96 and 2.05 µm and, one band at 2.55 µm. Pure gypsum exhibits one absorption band centered at 1.20 µm (due to H_2O combinations), a triplet of absorption bands of progressively decreasing intensity at 1.44, 1.49 and 1.53 µm (due to O-H stretches), and a band at 1.74 µm (due to an OH combination), a double band near 1.94 and 1.97 µm (due to H_2O combinations), a broad band centered at 2.2 µm constituted of two narrower components centered at 2.21 and 2.27 µm (due to H_2O combinations and/or S-O stretching overtones), and a band centered at 2.48 µm (due to S-O stretching combinations) [Cloutis et al., 2006; 2008]. When gypsum is mixed with water ice, the spectral behavior of the mixture may be described as follows.

- The gypsum absorption band at 1.20 µm is masked by the ice band at 1.25 µm even at high gypsum concentrations. Therefore the band at 1.20 µm cannot be used to detect gypsum when it is mixed with ice.

- Gypsum absorption bands remain visible at 1.44, 1.49 and 1.53 µm. However, the bands at 1.49 and 1.53 µm are small and are close to the center of the broad ice band at 1.50 µm. Therefore these two bands cannot be reliably discriminated from the 1.50 µm ice band. The 1.44

µm absorption band is sufficiently far from the center of the 1.50 µm ice band, that it remains visible at high gypsum concentrations and disappears progressively with increasing ice content.

- The gypsum absorption band at 1.74 µm turns into an inflexion at high gypsum concentrations and disappears at high ice concentrations.

- The 1.94 and 1.97 µm gypsum absorption bands remain visible even at high ice concentrations distorting the 2 µm water ice band.

- The broad gypsum absorption band at 2.2 µm disappears and only its two narrow components at 2.21 and 2.27 µm remain on the wings of the ice peak centered at 2.24 µm. At low gypsum concentrations, these two bands turn into residual inflexions on both sides of the ice peak.

- The 2.48 µm gypsum absorption band is close to the center of the broader 2.55 µm water ice band, and is therefore difficult to isolate.

To summarize, laboratory spectra show that, when gypsum is mixed with water ice, diagnostic gypsum absorption bands remain at 1.44, 1.74, 1.94, 2.21, 2.27 and 2.48 µm, but all of these bands are very shallow and may be overlapped by those of water ice. These bands are thus predictably difficult to detect in spectra acquired remotely of ice-rich regions on natural planetary surfaces. In addition, currently available Martian data are noisier than laboratory spectra and their spectral resolution is lower. We have therefore developed specific spectral processing methods to detect and to isolate these shallow diagnostic bands on Martian hyperspectral data.

4.2. Analysis of hyperspectral data in the study area

4.2.1. Data

The mineralogical composition of the study area was investigated from data acquired by the OMEGA and CRISM imaging spectrometers. We selected data acquired in summer (OMEGA cube ORB1056_2 and CRISM cube hrl0000330c) to minimize the contribution of the seasonal CO_2 and H_2O frost coverage.

OMEGA (Observatoire pour la Mineralogie, l'Eau, les Glaces et l'Activite) [Bibring et al., 2004], onboard Mars Express, acquires hyperspectral images at a spatial resolution ranging from 300 m to 4.8 km per pixel. A spectrum is acquired in 352 spectral channels from 0.38 to 5.2 µm for each pixel of an image, thus producing data cubes. CRISM (Compact Reconnaissance Imaging Spectrometer for Mars) [Murchie et al., 2007] is onboard Mars Reconnaissance Orbiter (MRO). In the targeted hyperspectral mode, CRISM collects 544 spectral channels from 0.36 to 3.9 µm at a spatial resolution ranging from 15 to 19 m/pixel.

We restricted our analysis to the spectral domain comprised between 1.0 and 2.5 µm. In this wavelength range, the solar reflected light dominates the spectrum, and the thermal emission is negligible [Gendrin et al., 2005]. This range is also suitable for the detection of hydrated minerals commonly identified on Mars, and is particularly diagnostic for gypsum. In order to avoid the effect of the CRISM smile [Murchie et al., 2007], we studied only the center of the image.

4.2.2. Extraction of the spectral information

4.2.2.1. Data reduction

OMEGA and CRISM spectra are acquired remotely through the atmosphere. In order to extract the spectral contribution of the surface only, the atmospheric spectral contribution is removed by using an empirical atmospheric transmission law derived from the ratio between two spectra acquired at the summit and the base of the Olympus Mons volcano, and scaled to the depth of the CO_2 band [Langevin et al., 2005a; McGuire et al., 2009]. The CRISM Analysis Toolkit (CAT) also corrects the photometric angles [Murchie et al., 2007]. Custom software routines are used to georeference the OMEGA and CRISM images in the Mars 2000 coordinate system with a polar stereographic projection.

4.2.2.2. Denoising

The experimental study of the spectral behavior of gypsum-ice mixtures described in part 4.1 suggests that most bands diagnostic of gypsum are close to the noise level in unprocessed Martian data. Different kinds of denoising procedures have thus been applied to CRISM and OMEGA data.

The CIRRUS tool, available in the CAT, was applied to the CRISM cube. CIRRUS first removes isolated noise spikes with the "despiking" tool and then corrects the column bias with the "destriping" tool [Parente, 2008]. We have also performed a Minimum Noise Fraction (MNF) transform on OMEGA and CRISM data. This procedure, available in the ENVI software, segregates the noise from the information in the data. An inverse MNF transform computed only on the components containing the information can be used to decrease the noise level in the data cube [Green et al., 1988].

4.2.2.3. Definition of spectral criteria

To identify spectral features (e.g. absorption bands, spectral slopes) that are diagnostic of minerals, we have computed spectral criteria. These correspond to combinations of reflectance measured at different wavelengths. In order to further decrease the contribution of noise when computing these spectral criteria, the reflectance at a given wavelength was taken as the median of the values of reflectance measured in three adjacent instrumental channels centered on this wavelength. Spectral criteria were computed for each pixel of a cube, and maps of each spectral criterion were then produced.

We mapped the distribution of water ice with the calculation of the 1.5 µm absorption band depth. This criterion is defined as follows:

$$BD(1.50) = 1 - \frac{R(1.50)}{(0.7) * R(1.37) + (0.3) * R(1.82)}$$

where R(x) is the value of reflectance corresponding to the wavelength at x µm.

On Mars, hydrated minerals such as gypsum have classically been identified with spectral criteria based on the depth of the 1.4 and 1.9 µm absorption bands [e.g. Pelkey et al., 2007; Massé et al., 2008]. However, these criteria cannot be used to detect hydrated minerals when they are mixed with ice because the broad 1.5 and 2.0 µm water ice bands overlap the 1.4 and 1.9 µm mineral hydration bands. Therefore, we used the criterion defined by Horgan et al. [2009] to isolate the 1.9 µm hydration band. This criterion is based on the assumption that the water ice band at 2.0 µm is symmetrical and that the addition of hydrated minerals imposes a slight asymmetry to this band. This criterion is defined as follows:

$$BD(1.934) = 1 - {CR1934}/{CR2108}$$

$$CR(x) = {R(x)}\Big/\left(\left[\frac{R(2.205)-R(1.842)}{2.205-1.842}\right](x-1.842)+R(1.842)\right)$$

The same method cannot be used to isolate the 1.4 µm hydration band from the 1.5 µm water ice band because the broad water ice band centered at 1.5 µm is not symmetrical. Similarly, the 2.21 and 2.27 µm gypsum absorption bands interfere with the ice peak centered at 2.24 µm. In addition, the 1.74, 2.21 and 2.27 µm gypsum bands appear as inflexions rather than as deep bands when gypsum is mixed with ice. Therefore all these bands, which are diagnostic of gypsum, cannot be detected by computing simple spectral criteria. Hence, we have therefore used a complementary method to monitor these specific shallows bands.

4.2.2.4. Spectral derivative method

Figure 6

The spectral derivative method has been initially developed to analyze terrestrial hyperspectral data. It allows one to determine the wavelength position of narrow bands and to resolve overlapping absorption bands [Huguenin and Jones, 1986; Talsky, 1994; Tsai and Philpot, 1998; Louchard et al., 2002, Verpoorter et al., 2007, Verpoorter, 2009; Verpoorter et al., 2010]. This method has the advantage of being less dependent on the shape of the continuum and thus removes background signals caused, for example, by differences in grain sizes or variations in topography and illumination conditions. The method is based on the principle that absorption bands constitute local minima in the spectrum (Fig. 6). They will therefore appear as zeros in the first order derivative of the spectrum and as maxima in its second order derivative. On the other hand, peaks between absorption bands constitute local maxima in the spectrum. They will therefore appear as zeros in the first order derivative and as minima in the second order derivative (Fig. 6). Inflexions will appear as local maxima or minima in the first order derivative and as zeros in the second order derivative (Fig. 6). By the systematic detection of local minima, local maxima and inflexions in a reflectance spectrum, the derivative method thus allows the identification of the exact center of absorption bands, even for shallow or overlapping ones, and independently from background signals. This technique enhances subtle fluctuations in reflectance spectra and separates closely related absorption features.

We have adapted this method to detect all local minima in hyperspectral cubes and to produce maps of their geographical distribution [Verpoorter, 2010]. The algorithm first detects the wavelengths of all local minima in the spectra of all pixels of a cube. Then it produces, for each identified wavelength, a map of the distribution of pixels where this wavelength corresponds to a local minimum. Finally, a density map is produced for each identified wavelength by counting, in a moving kernel (3x3), the number of pixels that display a local minimum at this wavelength.

4.3. Results

The histogram in Fig. 7 shows the frequency of all absorption bands detected by the spectral derivative method in the whole CRISM cube. Fig. 8 displays representative CRISM spectra of the morphological units described in part 3. Maps of spectral criteria and maps of absorption bands detected by the spectral derivative method are given in Fig. 9 and 10. Maps of spectral criteria provide quantitative information such as band depths, whereas maps derived from the spectral derivative method show the distribution of pixels where an absorption band is present at a given wavelength. The spectral derivative method enhances all the spectral fluctuations and is thus very sensitive. Therefore, overlapping absorption bands and weak spectral features that would not be detected by computing spectral criteria, are readily identified by the spectral derivative method. On the other hand, strong denoising must be performed before applying the spectral derivative method. In some cases, this denoising can lead to the loss of some of the faintest absorption bands. Our interpretation is therefore based on the joint analysis of both kinds of maps. To finally ensure that a given local minimum detected by the spectral derivative method corresponds to an absorption band rather than to residual noise, we check that pixels displaying this local minimum define a spatially and geologically consistent area.

4.3.1. Absorption bands detected in the study area

Figure 7

Fig. 7 shows the distribution of absorption bands that more than 50% of the pixels in the image display absorption bands centered at 1.50, 1.96 and 2.06 µm. Between 20% and 50% of the pixels display absorption bands at 1.07, 1.22, 1.37, 1.92, 2.14, 2.21 and 2.27 µm. Absorption bands are also detected at 1.30, 1.42, 1.57, 1.64, 1.73, 1.79, 1.86, 2.00 and 2.48 µm on less than 20% of the pixels.

4.3.2. Mineralogical interpretation

Figure 8
Figure 9

The absorption bands detected at 1.07, 1.22, 1.30, 1.50, 1.64, 1.96, 2.00 and 2.06 µm are consistent with those of water ice. However, the absorption bands at 1.96, 2.00 and 2.06 µm may be artifacts due to the fact that the CRISM atmospheric correction fails between 1.97 and 2.08 µm. The absorption bands at 1.22 and 1.64 µm could also correspond to CRISM artifacts and the absorption bands at 1.07 and 1.30 µm could be attributed to other components. We have thus only used the 1.50 µm absorption band to discriminate the water ice signature. This water ice absorption band appears most distinctly on clean ice layers of the NPLD (Fig. 8, 9a and 9d). The 1.50 µm water ice absorption band is also shallower on sediment-rich ice layers of the NPLD and on the polar and circum-polar superficial accumulations of dark sediment (Fig. 8, 9a and 9d). These include the sublimation till covering the surface below arcuate scarps, the arcuate scarps themselves, the sublimation till covering the dissected packet of NPLD ice layers described in part 3.4 and the dunes.

The absorption bands detected at 1.42, 1.73, 1.92, 2.21, 2.27 and 2.48 µm are consistent with those of gypsum mixed with ice, as we have identified them experimentally (Fig. 5). These gypsum absorption bands are spatially anti-correlated to those of water ice (Fig. 9). By contrast, they are correlated with the polar and circum-polar superficial accumulations of dark sediment (Fig. 8, 9b, 9c, 9e, 9f, 9g, 9h, 9i, 9j and 10). More specifically, they are present on the sublimation till covering the BU and the NPLD below arcuate scarps (Fig. 8, 10e and 10f), on the dunes (Fig. 8, 10e and 10f), on the dark streamers (Fig. 8, 10e and 10f), on the sediment-rich ice layers of the arcuate scarps (Fig. 8, 10e and 10f), and on the sublimation till covering the dissected packet of NPLD ice layers described in part 3.4 (Fig. 8, 10b and 10c).

The 1.42, 1.92, 2.21 and 2.27 µm gypsum absorption bands are well expressed on all of these superficial sedimentary accumulations (Fig. 9c, 9f, 9h and 9i) (corresponding to more than 20% of the pixels in the image, Fig. 7), while the 1.73 µm gypsum absorption band appears dominantly on sediment-rich layers of the arcuate scarps and on dune crests, and the 2.48 µm gypsum absorption bands appear dominantly on dune crests (Fig. 9e and 9j). As we have shown experimentally, this difference can be attributed to the fact that the gypsum/ice mixing ratio is higher in the dunes than in the sublimation tills. This interpretation is consistent with the observation in Olympia Planum that the strongest gypsum signature is located on dune crests rather than on interdunes [Roach et al., 2007; Calvin et al., 2009].

An absorption band centered at 2.14 µm is present on 30 % of the pixels in the image and is well visible both on raw and denoised CRISM spectral data (Fig. 7 and 8). This band is spatially correlated with the gypsum absorption bands and is characteristic of the dark polar and circum-polar sediment (Fig. 8 and 9g). Few common terrestrial minerals display an absorption band at this wavelength. This band could correspond to perchlorate, a mineral uncommon on Earth but that has been detected in the Martian permafrost at the Phoenix landing site [Hecht et al., 2009] and that displays a deep diagnostic absorption band at this wavelength [Hanley et al., 2009; Hanley et al., 2010; Morris et al., 2009]. It is interesting to notice that the possible presence of perchlorate could have some important implications on the flow of the North Polar Cap [Fisher et al., 2010]. As an alternative to perchlorate, the sulfite hannebachite ($2CaSO_3*H_2O$) has also a strong absorption band at 2.14 µm. As perchlorate has already been detected on Mars by the Phoenix lander, we favor perchlorate to interpret the absorption band at 2.14 µm. However, the presence of hannebachite cannot be ruled out since it would be consistent with the chemical model of Halevy and Schrag [2009] showing that SO2 on Mars prevents the formation of calcium carbonate in favor of this hydrated calcium sulfite.

Interestingly, gypsum and possibly perchlorate are present also in the bulk of sediment-rich ice layers of the NPLD. Absorption bands at 1.93, 2.21 (gypsum) and 2.14 µm (perchlorate?) are visible directly on spectra acquired on sediment-rich ice layers (Fig. 8) and spectral criterion BD(1.934) computed on raw data recognizes the 1.93 µm band on all the sediment-rich ice layers (Fig. 9b). With the spectral derivative method applied on denoised data, we detect the absorption bands at 1.93, 2.14 and 2.21 µm only in the most sediment-rich ice layers close to the dissected packet of NPLD (Fig. 9f, 10b and 10c), because these very shallow, narrow bands are easily erased by the the denoising procedure.

Other local minima detected by the spectral derivative method at 1.37, 1.57, 1.79 and 1.86 µm are more difficult to interpret. They might correspond to unidentified minerals or to spectral noise (Fig. 7).

4.3.3. Regional validation with OMEGA data

Figure 11
Figure 12

In order to validate the absorption bands detected in the study area and to check the consistency of these detections over a wider portion of the North Polar Cap, we applied the same processing methods to OMEGA data.

Spectra acquired on dunes and on sublimation tills covering the North Polar Cap display the same absorption bands, both on CRISM and OMEGA data (Fig. 11). This demonstrates that they have similar mineralogical compositions. The most subtle bands barely show up on OMEGA data however, due to the lower spatial resolution of the instrument, which induces higher spatial mixing. On a regional scale, absorption bands at 1.42, 1.92, 2.21 and 2.27 µm, which are diagnostic of gypsum, and an absorption band at 2.14 µm, which might be attributed to perchlorate, are found to be systematically correlated to sediment-rich areas (Fig. 12b, 12d, 12e, 12f and 12g) and anti-correlated with water ice-rich areas (Fig. 12a and 12c). These include the whole portion of the Circum-Polar Dune Field enclosed in the OMEGA cube and a significant number of pixels on the North Polar Cap, corresponding to sublimation tills, to arcuate scarps and to spiral troughs covered by superficial sediment (Fig. 12b, 12d, 12e, 12f and 12g).

5. Discussion

The mineralogical interpretation of CRISM and OMEGA hyperspectral data reveals that all kinds of polar and circum-polar superficial accumulations of dark sediment present in the study area (including sublimation tills at the surface of the North Polar Cap and dunes in the Circum-Polar Dune Field) display similar absorption bands (Fig. 8, 9, 10, 11 and 12). This indicates that they have similar mineralogical compositions. They are a mixture of ice and various minerals including gypsum and possibly perchlorate. Sediment with a similar composition is intermixed in the ice of the North Polar Cap. The interpretation of landforms in the study area reveals that the gypsum-bearing sediment present at the surface of the ice cap and in the Circum-Polar Dune Field was released from the ice cap by sublimation. We infer that gypsum crystals that are now present in the Circum-Polar Dune Field derive also from the North Polar Cap (Fig. 13). Dunes are necessarily composed of grains with a size of a few hundreds of microns [Bagnold, 1954]. This does not necessarily mean that the gypsum crystals derived from the ice cap must be so large. As suggested by Herkenhoff and Vasada [1999], the grains in the dunes may be composed of smaller gypsum crystals aggregated with ice and other minerals.

Figure 13

Two hypotheses remain for the ultimate origin of the gypsum crystals in the ice cap. (1) Pre-existing gypsum crystals might have been deposited together with ice crystals during the formation of the ice cap or (2) authigenic gypsum crystals might have grown within the ice cap by weathering of sediment trapped in the ice. We have no means to answer this question directly from currently available observations on Mars, but comparisons with terrestrial analogues might be meaningful.

Sulfate salt inclusions have been found in Greenland and Antarctica ice cores, with gypsum being the dominant salt species in layers deposited during glacial stages and Na- and/or Mg-sulfates being dominant in layers deposited during interglacial stages [Ohno et al., 2006]. The amount of each salt species in the ice depends on the ion balance and the priority sequence of chemical reactions. This priority sequence has been identified to be (1) calcium sulfate, (2) other sulfates, (3) nitrates, (4) chlorides and (5) carbonates [Iizuka et al., 2008]. Sulfate crystals, and particularly gypsum, are thus common in terrestrial glaciers. On Mars, the sequence of salts formation may be slightly different, but Tosca et al. [2006] demonstrated that gypsum is the first salt to form when $S0_4^{2-}$ is sufficiently abundant.

Sulfate crystals found in terrestrial glaciers can form in the atmosphere, prior to their deposition, by the neutralization of volcanic H_2SO_4 on dust containing Ca^{2+}, Na^+ or Mg^{2+} [Iizuka et al. 2006 and 2008]. Postdepositional processes also can affect the abundances and forms of ion species. These postdepositional processes include: (1) reworking and mixing of the surface snow by winds, (2) sublimation, condensation and volatilization in surface snow and (3) molecular diffusion in firn or ice. By this way, sulfate crystals can also form directly in the ice when liquid-phase SO_4^{2-} diffuses to relatively immobile Ca^{2+}, Na^+ or Mg^{2+} [Iizuka et al., 2006; 2008].

To conclude, sulfate crystals that are present in the Earth's closest cold-desert analogs for the Martian North Polar Cap, have probably formed both in the atmosphere and in the ice [Iizuka et al., 2006 and 2008]. By the same way, gypsum crystals that are present in the North Polar Cap of Mars may be both: (1) pre-existing gypsum crystals that have formed in the atmosphere and have been deposited together with ice crystals during the formation of the ice cap and (2) authigenic gypsum crystals that have formed in the ice cap by post-depositional processes.

A genetic link between sulfates and ice bodies has been suggested previously to explain the formation of ancient sulfate deposits in equatorial regions of Mars [Niles and Michalski, 2009]. These authors argue that ice bodies with intermixed sediment, similar to the Polar Layered Deposits that are currently present in the North and South Polar Caps, have formed in equatorial regions of Mars during former periods of high obliquity or polar wander. Within these massive ice deposits, acid weathering of the intermixed sediment would have led to the formation of sulfates. Later, aeolian reworking of the sublimation residue of this mixture of ice and sulfates would have formed the equatorial sulfate-bearing sediments. This model is consistent with recent results of thermodynamical models, which indicate that low-temperature acid weathering of basaltic dust with small amounts of liquid water can lead to the formation of sulfates in a few decades only [Berger et al., 2009]. According to Niles and Michalski [2009], their ice-weathering model resolves many chemical and morphological problems highlighted by previous hypotheses concerning the formation of equatorial sulfates on the Martian surface. In equatorial regions, the ancient accumulations of intermixed ice and sediment required by the model have disappeared. Therefore, the ice-weathering model is difficult to evaluate directly in these regions. Our results however demonstrate that recent polar and circum-polar sulfate deposits derive from the North Polar Cap and thus support the possibility that similar processes may have occurred at lower latitudes in the past.

6. Conclusion

The development of a spectral processing method based on spectral derivation allows resolving overlapping absorption bands between water ice and sediment in the North Polar Cap and in the Circum-Polar Dune Field. We find that the hydrated minerals detected by Horgan et al. [2009] and Calvin et al. [2009] in the study area correspond to gypsum and possibly perchlorate. Therefore, the presence of gypsum is not restricted to the Olympia Planum dunes but can probably be extended to the whole Circumpolar Dune Field. Gypsum is also found on all the superficial sediment present in the study area including: sublimation tills at the surface of the NPLD and the BU, sediment-rich ice layers and dark streamers released from the polar cap. We thus deduce that circumpolar gypsum has not formed by in-situ weathering of the dunes but was initially present in the North Polar Cap and has been released to the surface by the ablation of the ice. This morphological and mineralogical study also shows that sediment constituting the circumpolar dunes originates both from the NPLD and the BU. The proportion of sediment intermixed with ice is smaller in the NPLD than in the BU [Picardi et al., 2005; Phillips et al., 2008], therefore the majority of the dune material is probably provided by the BU.

According to these results we propose the following scenario for the formation of polar and circum-polar sulfate-bearing deposits on Mars (Fig. 13).

1. Gypsum crystals form in the atmosphere and/or in the ice cap by neutralization of volcanic H2SO4 on Ca-bearing sediment.
2. These gypsum crystals are trapped in the ice.
3. Erosion of the ice cap by winds and sublimation leads to the formation of spiral troughs, arcuate scarps and other ablation landforms.

4. As erosion proceeds, gypsum crystals are released from the ice and they concentrate in sublimation tills at the surface of the ice cap.

5. Gypsum-bearing sublimation tills are reworked by winds and transported towards the Circum-Polar Dune Field.

This scenario is consistent with the observation of sulfate crystals, and particularly gypsum, in Greenland and Antarctic ices cores, which form both by predepositional processes in the atmosphere and postdepositional processes in the ice [Ohno et al., 2006; Iizuka et al., 2006 and 2008]. It may also provides a basis, derived from the analysis of processes recently active in the polar regions of Mars, to constrain the processes that were responsible for the formation of sulfate-bearing deposits at lower latitudes in the past.

Acknowledgments

This work benefited from financial supports from the Centre National de la Recherche Scientifique, Institut National des Sciences de l'Univers (Programme National de Planétologie),

ACCEPTED MANUSCRIPT

and from the Centre National d'Etudes Spatiales. M. Massé is supported by a Ph.D. research grant from the French government (Ministère de l'Enseignement Supérieur et de la Recherche). We thank Cécile Taffin for her help with the cryostat. We thank L. Roach and an anonymous reviewer for their insightful comments. Thorough advising from Nicolas Mangold and Stéphane Pochat greatly improved the quality of this article.

References

Arvidson, R.E., and 25 colleagues (2006), Overview of the Spirit Mars Exploration Rover Mission to Gusev Crater: Landing site to Backstay Rock in the Columbia Hills, J. of Geophys. Res., 111, E02S01, doi:10.1029/2005JE002499.

Bagnold, R.A. (1954), The physic of blown sand and desert dunes, Dover Publications, 265 p.

Berger, G., M.J. Toplis, E. Treguier, C. d'Uston and P. Pinet (2009), Evidence in favor of small amounts of ephemeral and transient water during alteration at Meridiani Planum, Mars, American Mineralogist, 94, 1279-1282.

Betterton, M.D. (2001), Theory of structure formation in snowfields motivated by penitentes, suncups, and dirt cones, Physical Review E, 63, 056129.

Bibring, J-P., and 42 colleagues (2004), OMEGA : Observatoire pour la Minéralogie, l'Eau, les Glaces et l'Activité, Eur. Space Agency Spec. Publ. 1240, 37.

Byrne, S. and B.C. Murray (2002), North polar stratigraphy and the paleo-erg of Mars, J. of Geophys. Res., 107, E6, 5044, doi: 10.1029/2001JE001615.

Byrne, S., M.T. Zuber, G.A. Neumann (2008), Internannual and seasonal behavior of Martian residual ice-cap albedo, Planet. and Sp. Sci., 56, 194-211.

Calvin, W.M., L.H. Roach, F.P. Seelos, K.D. Seelos, R.O. Green, S.L. Murchie, J.F. Mustard (2009), CRISM Observations of the Northern Martian Latitudes in Summer, J. of Geophys. Res., 114, E00D11, doi:10.1029/2009JE003348.

Carr, M.H. and J.W. Head (2009), Geologic history of Mars, Earth and Planet. Sci. Lett., doi:10.1016/j.epsl.2009.06.042.

Catling, D.C. (1999), A chemical model for evaporites on early Mars: Possible sedimentary tracers of the early climate and implications for exploration, J. of Geophys. Res., 104, 16,453-16,469.

Chevrier, V. and P.E. Mathé, (2007), Mineralogy and evolution of the surface of Mars: a review, Planet. and Sp. Sci., 55, 289-314.

Christensen, P.R., and 26 colleagues (2004), Mineralogy at Meridiani Planum from the Mini-Tes experiment on the Opportunity rover, Science, 306, 1733-1739.

Cloutis, E.A., and 11 colleagues (2006), Detection of sulfate minerals using reflectance spectroscopy, Icarus, 184, 121-157.

Cloutis, E.A., M.A. Craig, R.V. Kruzelecky, W.R. Jamroz, A. Scott, F.C. Hawthorne, S.A. Mertzman (2008), Spectral reflectance properties of minerals exposed to simulated Mars surface conditions, Icarus, 195, 140-168.

Dupire, C., E. Le Menn, O. Grasset and S. Le Mouélic (2009), In situ infrared studies of water and CO2 frost between 1 and 5 µm : from the grain to the icy surfaces signatures, 40th LPS, Abstract 1242.

Edgett, K.S., R.M.E. Williams, M.C. Malin, B.A. Cantor, P.C. Thomas (2003), Mars landscape evolution: influence of stratigraphy in the north polar region, Geomorphology, 52, 289-297.

Fishbaugh, K.E. and J.W. Head III (2000), North polar region of Mars: Topography of circum-polar deposits from Mars Orbiter Laser Altimeter (MOLA) data and evidence for asymmetric retreat of the polar cap, J. of Geophys. Res., 105, 22,455-22,486.

Fishbaugh, K.E. and J.W. Head III (2005), Origin and characterisitics of the Mars north polar basal unit and implications for polar geologic history, Icarus, 174, 444-474.

Fishbaugh, K.E., F. Poulet, V. Chevrier, Y. Langevin and J.-P. Bibring (2007), On the origin of gypsum in the Mars north polar region, J. of Geophys. Res., 112, E07002, doi:10.1029/2006JE002862.

Fishbaugh, K.E., C.S. Hvidberg, D. Beaty, S. Clifford, D. Fisher, A. Haldemann, J.W. Head, M. Hecht, M. Koutnik, K. Tanaka, W.J. Ammann (2008), Introduction to the 4th Mars Polar Science and Exploration Conference special issue: Five top questions in Mars polar science, Icarus, 196, 305-317.

Fisher, D.A., M.H. Hecht, S.P. Kounaves and D.C. Catling (2010), A perchlorate brine lubricated deformable bed facilitating flow of the north polar cap of Mars: possible mechanism for water table recharging, J. of Geophys. Res., 115, E00E12, doi:10.1029/2009JE003405.

Fountain, A.G., T.H. Nylen, K.L. MacClune, G.L. Dana (2006), Glacier and mass balances (1993-2001), Taylor Valley, McMurdo Dry Valleys, Antarctica, Journal of Glaciology, 52, no 178.

Gendrin, A., N. Mangold, J.-P. Bibring, Y. Langevin, B. Gondet, F. Poulet, G. Bonello, C. Quantin, J. Mustard, R. Arvidson and S. Le Mouélic (2005), Sulfates in Martian layered terrains : the OMEGA/Mars Express view, Science, 307, 1587-1591.

Green, A.A., M. Berman, P. Switzer, and Craig, M.D. (1988), A transformation for ordering multispectral data in terms of image quality with implications for noise removal: IEEE, Transactions on Geoscience and Remote Sensing, 26, no. 1, p. 65-74.

Halevy, I., and D.P. Schrag (2009), Sulfur dioxide inhibits calcium carbonate precipitation: implications for early Mars and Earth, Geophys. Res. Lett., 36, L23201, doi:10.1029/ 2009GL040792.

Hanley, J., V.F. Chevrier, B.L. Davis, T.S. Altheide, A. Francis (2009), Reflectance spectra of low-temperature chloride and perchlorate hydrates and thier relevance to the martian surface, The New Martian Chemistry Workshop, abstract 8010.

Hanley, J., V.F. Chevrier, B.L. Davis, T.S. Altheide, A. Francis (2010), Reflectance spectra of low-temperature chloride and perchlorate hydrates and their relevance to the martian surface, 41st Lunar and Planetary Science Conference, Abstract 1953.

Hayward, R.K., K.F. Mullins, L.K. Fenton, T.M. Hare, T.N. Titus, M.C. Bourke, A. Colaprete and P.R. Christensen (2007), Mars Global Digital Dune Database and initial science results, J. of Geophys. Res., 112, E11007, doi:10.1029/2007JE002943.

Hecht, M.H., and 13 colleagues (2009), Detection of Perchlorate and the Soluble Chemistry of Martian Soil at the Phoenix Lander Site, Science, 325, 64, doi: 10.1126/science.1172466.

Herkenhoff, K.E., S. Byrne, P.S. Russel, K.E. Fishbaugh, A.S. McEwen (2007), Meter-scale morphology of the North Polar Region of Mars, Science, 317, 1711-1715, doi: 10.1126/science.1143544.

Herkenhoff, K.E., A.R. Vasada (1999), Dark material in the polar layered deposits and dunes on Mars, J. of Geophys. Res., 104, 16,487-16,500.

Hoffman, M.J., A.G. Fountain and G.E. Liston (2008), Surface energy balance and melt thresholds over 11 years at Taylor Glacier, Antarctica, J. of Geophys. Res., 113, F04014, doi: 10.1029/2008JF001029.

Horgan, B.H., J.F. Bell III, E.Z. Noe Dobrea, E.A. Cloutis, D.T. Bailey, M.A. Craig, L.H. Roach, and J. F. Mustard (2009), Distribution of hydrated minerals on the north polar region of Mars, J. of Geophys. Res., 114, E01005, doi:10.1029/2008JE003187,

Horgan, B.H. and J.F. Bell III (2009), Insights from ferrous mineralogy into the transport of martian north polar materials, 40th LPSC, Abstract 2457.

Howard, A.D. (2000), The role of eolian processes in forming surface features of the Martian Polar Layered Deposits, Icarus, 144, 267-288, doi: 10.1006/icar.1999.6305.

Howard, A.D., J.A. Cutts, K.R. Blasius (1982), Stratigraphic relationships within Martian polar cap deposits, Icarus, 50, 161-215.

Huguenin, R.L. and J.L. Jones (1986), Intelligent information extraction from reflectance spectra: absorption band positions, J. of Geophys. Res., 91, 9585-9598.

Ivanov, A.B. and D.O. Muhleman (2000), The roles of sublimation for the formation of the northern ice cap: results from the Mars Orbiter Laser Altimeter, Icarus, 144, 436-448.

Iizuka, Y., T. Hondoh, Y. Fujii (2006), Na_2SO_4 and $MgSO_4$ salts during the Holocene period derived by high-resolution depth analysis of a Dome Fuji ice core, Journal of Glaciology, 52, No. 176.

Iizuka, Y., S. Horikawa, T. Sakurai, S. Johnson, D. Dahl-Jensen, J.P. Steffensen, and T. Hondoh (2008), A relationship between ion balance and the chemical compounds of salt inclusions found in the Greenland Ice Core Project and Dome Fuji ice cores, J. of Geophys. Res., 113, D07303, doi:10.1029/2007JD009018.

Kieffer, H.H., S.C. Chase, T.Z. Martin, E.D. Miner and F. Don Palluconi (1976), Martian North Pole summer temperature: dirty water ice, Science, 194, 1341-1344.

Langevin, Y., F. Poulet, J.-P. Bibring, B. Schmitt, S. Douté, B. Gondet (2005a), Summer evolution of the North Polar Cap of Mars as observed by OMEGA/Mars Express, Science, 307, 1581-1584.

Langevin, Y., F. Poulet, J.-P. Bibring, J.-P. Bibring and B. Gondet (2005b), Sulfates in the North Polar Region of Mars detected by OMEGA/Mars Express, Science, 307, 1584-1586.

Le Deit, L., S. Le Mouélic, D. Mège, O. Bourgeois, J.-P. Combe, C. Sotin, A. Gendrin, E. Hauber, N. Mangold and J.-P. Bibring (2008), Ferric oxides in East Candor Chasma, Valles

Marineris (Mars) inferred from analysis of OMEGA/Mars Express data: identification and geological interpretation, J. of Geophys. Res., 113, Issue E7, doi:10.1029/2007JE002950.

Louchard, E.M., R.P. Reid, C.F. Stephens, C.O. Davis, R.A. Leathers, T.V. Downes, R. Maffione (2002), Derivative analysis of absorption features in hyperspectral remote sensing data of carbonate sediments, Optics Express, 1573.

Malin, M.C., and 13 colleagues (2007), Context Camera Investigation on board the Mars Reconnaissance Orbiter, J. of Geophys. Res., 112, E05S04, doi: 10.1029/2006JE002808.

Massé, M., S. Le Mouélic, O. Bourgeois, J.-P. Combe, L. Le Deit, C. Sotin, J.-P. Bibring, B. Gondet and Y. Langevin (2008), Mineralogical composition, structure, morphology, and geological history of Aram Chaos crater fill on Mars derived from OMEGA Mars Express data, J. of Geophys. Res., 113, E12006, doi:10.1029/2008JE003131.

McEwen, A.S., and 14 colleagues (2007), Mars Reconnaissance Orbiter's High Resolution Imaging Science Experiment (HiRISE), J. of Geophys. Res., 112, E05S02, doi:10.1029/2005JE002605.

McGuire, P.C., and 14 colleagues (2009), An improvement to the volcano-scan algorithm for atmospheric correction of CRISM and OMEGA spectral data, Planet. Sp. Sci., 57, 809-815.

McKee, E.D. (1979), Introduction to a study of global sand seas, in A study of global sand seas, U.S. Geological Survey Professional Paper, 400p.

Milkovich, S.M. and J.W. Head (2006), Surface textures of Mars' north polar layered deposits: A framework for interpretation and future exploration, Mars 2, 21-45.

Mölg T., D.R. Hardy and G. Kaser (2003), Solar-radiation-maintained glacier recession on Kilimanjaro drawn from combined ice-radiation geometry modelling, J. of Geophys. Res., 108, D23, 4731, doi:10.1029/2003JD003546.

Mölg T.and D.R. Hardy (2004), Ablation and associated energy balance of a horizontal glacier surface on Kilimanjaro, J. of Geophys. Res., 109, D16104, doi: 10.1029/2003JD004338.

Mölg T., N.J. Cullen, D.R. Hardy, G.Kaser and L. Klok (2008), Mass balance of a slope glacier on Kilimanjaro and its sensitivity to climate, International Journal of Climatology, 28, 881-892.

Morris, R.V., D.C. Golden, D.W. Ming, T.G. Graff, R.E. Arvidson, S.M. Wiseman, K.A. Lichtenberg and S. Cull (2009), Visible and near-IR reflectance spectra for smectite, sulfate and perchlorate under dry conditions for interpretation of martian surface mineralogy, 40th LPSC, Abstract 2317.

Murchie, S.R., and 49 colleagues (2007), Compact reconnaissance imaging spectrometer for Mars (CRISM) on Mars Reconnaissance Orbiter (MRO), J. of Geophys. Res., 112(E5), E05S03, doi:10.1029/2006JE002682.

Niles, P. and J. Michalski (2009), Meridiani Planum sediments on Mars formed through weathering in massive ice deposits, Nature Geoscience, 2, 215 – 220.

Ohno, H., M. Igarashi, and T. Hondoh (2006), Characteristics of salt inclusions in polar ice from Dome Fuji, East Antartica, Geophys. Res. Lett., 113, L08501, doi: 10.1029/2006GL025774.

Parente, M. (2008), A new approach to denoising CRISM images, Lunar and Planetary Science XXXIX, Abstract 2528.

Pelkey, S.M., J.F. Mustard, S. Murchie, R.T. Clancy, M. Wolff, M. Smith, R. Milliken, J.-P. Bibring, A. Gendrin, F. Poulet, Y. Langevin and B. Gondet (2007), CRISM multispectral summary products: Parameterizing mineral diversity on Mars from reflectance, J. of Geophys. Res., 112, E08S14, doi:10.1029/2006JE002831.

Picardi, G ., and 33 colleagues (2005), Radar sounding of the subsurface of Mars, Science, 310, 1925-1928.

Phillips, R.J., and 26 colleagues (2008), Mars north polar deposits: stratigraphy, age, and geodynamical response, Science, 320, 1182-1185.

Poulet, F., Y. Langevin, G. Boubin, D. Jouglet, J.-P. Bibring and B. Gondet (2008), Spectral variability of the Martian high latitude surfaces, Geophys. Res. Lett., 35, L20201, doi:10.1029/2008GL035450.

Putzig, N.E., R.J. Phillips, B.A. Campbell, J.W. Holt, J.J. Plaut, L.M. Carter, A.F. Egan, F. Bernardini, A. Saefaeinili, R. Seu (2009), Subsurface structure of Planum Boreum from Mars Reconnaissance Orbiter shallow radar soundings, Icarus, doi: 10.1016/j.icarus.2009.07.034.

Rhodes, J.J., R.L. Armstrong, S.G. Warren (1987), Mode of formation of “ablation hollows” controlled by dirt content of snow, Journal of Glaciology, 33, 135-139.

Roach, L.H., and 16 colleagues (2007), CRISM spectral signatures of the North polar gypsum dunes, LPSC XXXVII, abstract 1970.

Roach, L.H., J.F. Mustard, S.L. Murchie, J.-P. Bibring, F. Forget, K.W. Lewis, O. Aharonson, M. Vincendon and J.L. Bishop (2009), Testing evidence of recent hydration state change in sulfates on Mars, J. of Geophys. Res., 114, E00D02, doi: 10.1029/2008JE003245.

Rodriguez, J.A.P., K.L. Tanaka, Y. Langevin, M. Bourke, J. Kargel, P. Christensen and S. Sasaki (2007), Recent aeolian erosion and deposition in the north polar plateau of Mars, Mars 3, 29-41.

Rouchy, J.-M. and Blanc-Valleron M.-M. (2006), Les évaporites : Matériaux singuliers, milieux extrêmes, Vuibert, 190 p.

Smith, D.E., and 21 colleagues (2001a), Mars Orbiter Laser Altimeter (MOLA): Experiment summary after the first year of global mapping of Mars, J. of Geophys. Res., 106, 23689-23722.

Smith, D.E., M.T. Zuber, G.A. Neumann (2001b), Seasonal variations of snow depth on Mars, Science, 294, no. 5549, 2141-2146.

Squyres, S.W., and 15 colleagues (2006), Rocks of the Columbia Hills,, J. of Geophys. Res., 111, E02S11, doi:10.1029/2005JE002562.

Szynkiewicz, A., R.C. Ewing, C.H. Moore, M. Glamoclija, D. Bustos, L.M. Pratt (2010), Origin of terrestrial gypsum dunes-Implications for Martian gypsum-rich dunes of Olympia Undae, Geomorphology, in press, DOI: 10.1016/j.geomorph.2009.02.017.

Talsky, G. (1994), Derivative Spectrophotometry, low and high order, VCH Publishers.

Tanaka, K.L., J.A.P. Rodriguez, JA. Skinner, M.C. Bourke, C.M. Fortezzo, K.E. Herkenhoff, E.J. Kolb, C.H. Okubo (2008), North polar region of Mars: Advances in stratigraphy, structure, and erosional modification, Icarus, 196, 318-358.

Tanaka, K.L. and R.K. Hayward (2008), Mars' North circum-polar dunes: distribution, sources, and migration history, Planetary Dunes Workshop: A record of climate change, abstract 7012.

Thomas, P. and C. Weitz (1989), Sand dune materials and polar layered deposits on Mars, Icarus, 81, 185-215.

Tsai, F., and W. Philpot (1998), Derivative analysis of hyperspectral data, Remote Sensing of Environment, 66(1), 41-51.

Tsoar, H., R. Greeley, A.R. Peterfreund (1979), Mars: the north polar sand sea and related wind patterns, J. of Geophys. Res., 84, 8167-8180.

Verpoorter, C., V. Carrère, M. Robin (2007), Retrieval of physical properties of mudflat sediments from hyperspectral data using the modified gaussian model and spectral curve fitting, Proceedings 5th EARSeL Workshop on Imaging Spectroscopy.

Verpoorter, C. (2009), Teledetection hyperspectrale et cartographie des facies sedimentaires en zone intertidale: application a la baie de Bourgneuf, PhD, University of nantes, 423p.

Verpoorter, C., J.P., Combe and V., Carrere (2010), Development of an automatic Spectral Derivative - Modified Gaussian Model (SD-MGM) for the analysis of bio-geophysical properties of mudflat sediments from hyperspectral data, submitted in Remote Sensing of Environment.

Warner, N.H. and J.D. Farmer (2008), Importance of Aeolian processes in the origin of the north polar chasmata, Mars, Icarus, 196, 368-384.

Wray, J.J., S.L. Murchie, S.W. Squyres, F.P. Seelos and L.L. Tornabene (2009), Diverse aqueous environments on ancient Mars revealed in the southern highlands, Geology, 37, 1043-1046.

Zuber, M., and 20 colleagues (1998), Observations of the north polar region of Mars from the Mars Orbiter Laser Altimeter. Science, 282, 2053–2060.

Figure captions

Figure 1: a) Topographic map of the North Polar Cap (shaded and colored relief image computed from the MOLA DEM at ~512 m/pixel overlain on a MOC mosaic at ~221 m/pixel). The orange dotted line represents the extension of the Basal Unit (BU) inferred from radar soundings by Putzig et al. [2009]. b) Map of gypsum concentration in the Circum-Polar Dune Field, computed from 11 OMEGA observations by Langevin et al. [2005b]. The North Polar Cap appears in white and grey, whereas the Circum-Polar Dune Field appears in black. Colors indicate the depth of the 1.927 µm absorption band, interpreted as a proxy for the distribution of gypsum. c) Interpretative cross-section of the North Polar Cap based on SHARAD radargrams [Putzig et al., 2009]. The dotted line indicates the top of the Vastitas Borealis Formation (VBF), as interpreted from scarce radar returns.

Figure 2: Context map of the study area (shaded and colored relief image computed from the MOLA DEM at ~512 m/pixel overlain on a CTX mosaic; location indicated by a grey box in Figure 1). Topographic contours drawn at 200 m intervals underline the interior spiral troughs and the marginal arcuate scarps. The Circum-Polar Dune Field appears as a low-albedo unit, whereas ice appears as light outcrops. The study area (red box) encompasses the surface of the North Polar Cap, two spiral troughs, two arcuate scarps and a portion of the Circum-Polar Dune Field. The orange dotted line represents the extension of the Basal Unit (BU) inferred from radar soundings by Putzig et al. [2009].

Figure 3: Structure and morphology of the study area. a) CTX image P01_001593_2635_XI_83N241W (location indicated by a red box on Figure 2). b) Interpretative

sketch-map of Figure 3a. The interval of MOLA elevation contours is 100m. c) Close-up view of the northernmost arcuate scarp, showing the NPLD in its upper part, the BU in its lower part and superficial dark streamers extending from its base towards the associated dune field (location indicated by a black box on Figure 3a). d) Interpretative cross-section of the study area (location on Figure 3a and b). The topographic profile is based on MOLA DTM.

Figure 4: a) Sublimation landforms observed on a dissected packet of sediment-rich ice layers in the NPLD (Portion of HiRISE image PSP_009267_2640, location indicated by a black box in Figure 3a). The extent of the superficial ablation till released by sublimation of the packet of ice layers is delineated by the white dotted line. b) Close-up view on sublimation till and polygonal ablation hollows at the surface of the packet of ice layers (location indicated by the white box in Figure 4a). c) Example of terrestrial ablation hollows with concentration of ablation till on ridges at the surface of the Vatnajökull glacier in Iceland (20 cm long hammer for scale) (photo M. Massé). d) Interpretative block diagram illustrating the internal structure of the packet of ice layers and the surface sublimation landforms produced by downward ablation of the ice layers.

Figure 5: Laboratory spectra of experimental water ice - gypsum mixtures acquired at 150 K and 7 mbar. Grey and black dotted vertical bars underline spectral features attributed to water ice and gypsum respectively.

Figure 6: First order (R'(x)) and second order (R''(x)) derivatives of a portion of a CRISM spectrum (R(x)).

Figure 7: Distribution of absorption bands detected by the spectral derivative method in the CRISM cube hrl0000330c. The most geologically plausible mineralogical interpretation is indicated above each frequency peak.

Figure 8: Representative spectra of various morphological units of the study area. The central image is a color composition (R: 2.5295 µm, V: 1.5066 µm, B: 1.0800 µm) of the study area computed from CRISM cube hrl0000330c (location indicated by a grey box on Figure 2). Clean ice layers appear in blue, sediment-rich ice layers appear in white, superficial sublimation tills appear in various tones ranging from pale to medium brown and dunes appear in dark brown. Raw (grey) and denoised (black) spectra derived from this CRISM cube are shown to the left and right of the image. The reflectance values are given for the denoised spectra. For clarity, each raw spectrum is offset by a constant reflectance value with respect to the corresponding denoised spectrum. Grey and black dotted vertical bars underline spectral features attributed to ice and sediment respectively. To decrease the contribution of noise on the displayed spectra, these have been averaged over boxes (shown in the image) comprising several pixels located on the same morphological unit. All the spectra have been masked between 1.97 and 2.08 µm because the atmospheric correction fails in this wavelength range.

Figure 9: Distribution of ice, gypsum and other hydrated minerals in the study area, computed from the CRISM cube hrl0000330c. a) Map of the spectral criterion BD(1.50). b) Map of the spectral criterion BD(1.934). c) to j) Maps of selected absorption bands detected by the spectral derivative method. On c) to j), pixels where the spectrum meets a local minimum at the displayed wavelength are colored. Colors represent the number of pixels (1 to 9 pixels from blue to red) where this minimum is detected in a moving kernel of 3x3 pixels.

Figure 10: Zooms on the CTX image P01_001593_2635_XI_83N241W (location indicated on Figure 9a) and on maps of absorption bands detected by the spectral derivative method (Figure 9), showing the concentration of gypsum in a) to c) sublimation tills on the dissected packet of the NPLD ice layers and in d) to f) arcuate scarp and dunes.

Figure 11: Comparison of (denoised) CRISM and (raw) OMEGA spectra acquired on superficial accumulations of dark sediment in the study area (location indicated on Figure 8). To ensure consistency of spatial coverage between CRISM and OMEGA data, the displayed CRISM spectra have been averaged over spatial boxes corresponding to the ground coverage of OMEGA pixels. Grey and black dotted vertical lines underline spectral features attributed to ice and sediment respectively.

Figure 12: Regional distribution of ice, gypsum and other hydrated minerals around the study area (shown by the white box in a), computed from the OMEGA cube ORB1056_2. a) Map of the spectral criterion BD(1.50). b) Map of the spectral criterion BD(1.934). c) to g) Maps of selected absorption bands detected by the spectral derivative method. On c) to g), pixels where the spectrum meets a local minimum at the displayed wavelength are colored. Colors represent the number of pixels (1 to 9 pixels from blue to red) where this minimum is detected in a moving kernel of 3x3 pixels. h) Location of the OMEGA cube indicated on a shaded and colored relief image computed from the MOLA DEM at ~256 m/pixel.

Figure 13: Interpretative scenario for the formation of gypsum in the North Polar Cap.

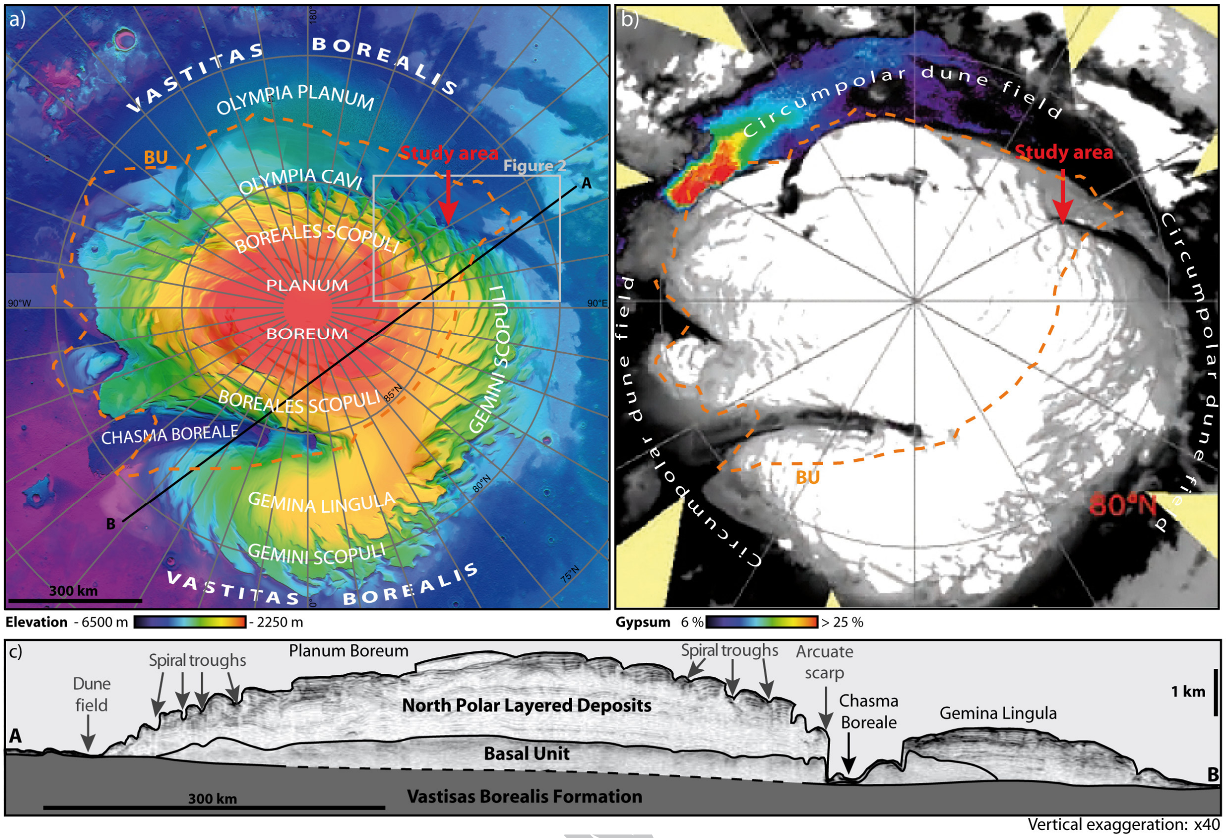
a)
VASTITAS BOREALIS
OLYMPIA PLANUM
BU
Study area
Figure 2
OLYMPIA CAVI
BOREALES SCOPULI
PLANUM
BOREUM
90°W
90°E
180°
GEMINI SCOPULI
BOREALES SCOPULI
85°N
CHASMA BOREALE
80°N
GEMINA LINGULA
GEMINI SCOPULI
75°N
A
B
300 km
VASTITAS BOREALIS
Elevation - 6500 m - 2250 m
b)
Circumpolar dune field
Study area
BU
80°N
Gypsum 6 % > 25 %
c)
Spiral troughs
Planum Boreum
Spiral troughs
Arcuate scarp
Dune field
North Polar Layered Deposits
Chasma Boreale
Gemina Lingula
1 km
A
Basal Unit
B
300 km
Vastisas Borealis Formation
Vertical exaggeration: x40

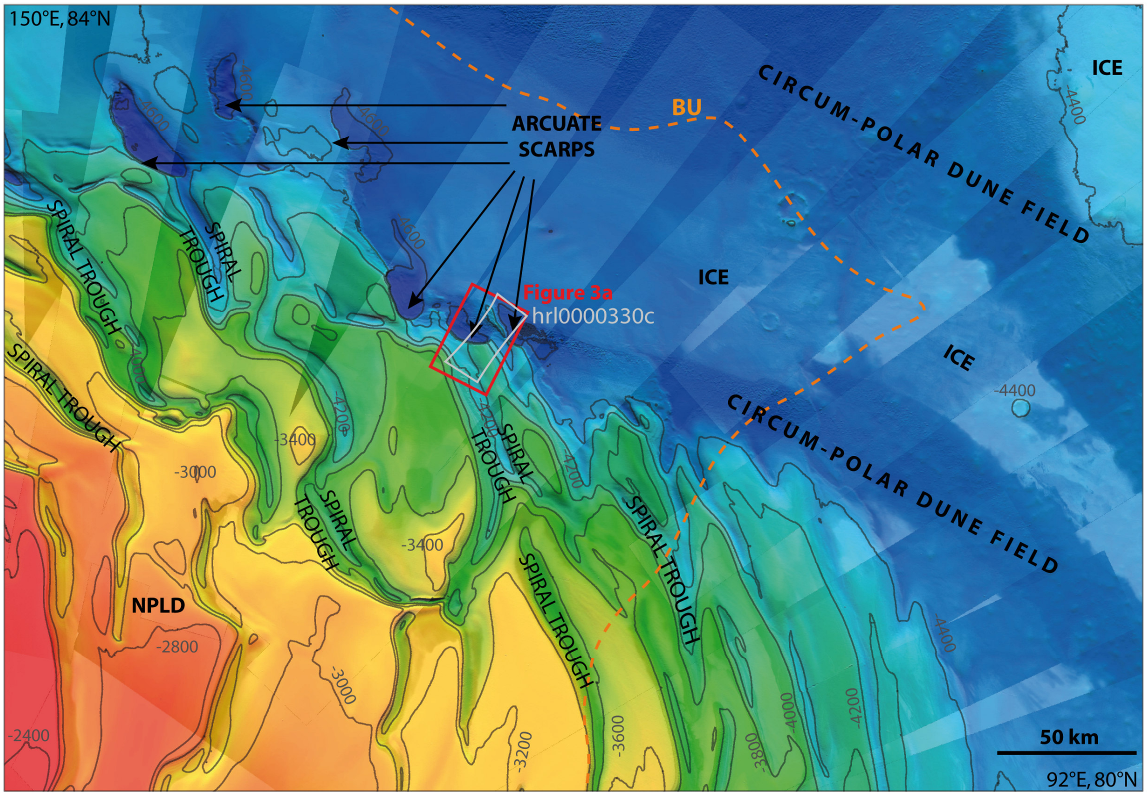
150°E, 84°N
ICE
BU
CIRCUM-POLAR DUNE FIELD
ARCUATE SCARPS
SPIRAL TROUGH
SPIRAL TROUGH
SPIRAL TROUGH
Figure 3a
hrl0000330c
ICE
ICE
-4400
CIRCUM-POLAR DUNE FIELD
SPIRAL TROUGH
SPIRAL TROUGH
SPIRAL TROUGH
SPIRAL TROUGH
-3400
-3000
-3400
NPLD
-2800
-3000
-2400
-3200
-3600
-3800
-4000
-4200
-4400
50 km
92°E, 80°N

1133

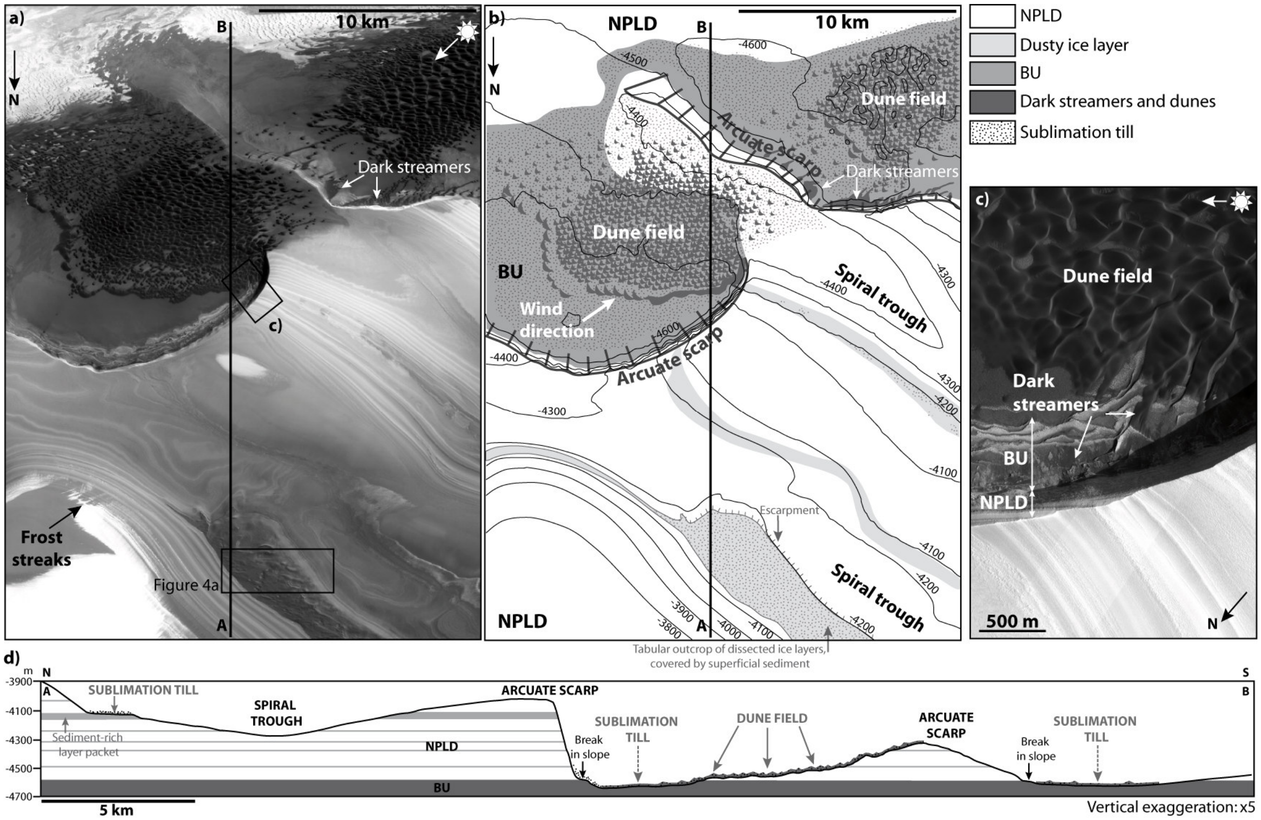
a)
B
10 km
N
Dark streamers
c)
Frost streaks
Figure 4a
A
b)
NPLD
B
10 km
N
-4600
-4500
-4400
Arcuate scarp
Dune field
Dark streamers
BU
Dune field
Wind direction
Spiral trough
-4300
-4400
-4600
Arcuate scarp
-4300
-4200
-4100
-4100
Escarpment
-4200
Spiral trough
NPLD
-3900
-3800
-4000
-4100
-4200
A
Tabular outcrop of dissected ice layers, covered by superficial sediment
NPLD
Dusty ice layer
BU
Dark streamers and dunes
Sublimation till
c)
Dune field
Dark streamers
BU
NPLD
500 m
N
d)
m
N
S
A
B
-3900
-4100
-4300
-4500
-4700
SUBLIMATION TILL
Sediment-rich layer packet
SPIRAL TROUGH
ARCUATE SCARP
NPLD
BU
Break in slope
SUBLIMATION TILL
DUNE FIELD
ARCUATE SCARP
Break in slope
SUBLIMATION TILL
5 km
Vertical exaggeration: x5

1135 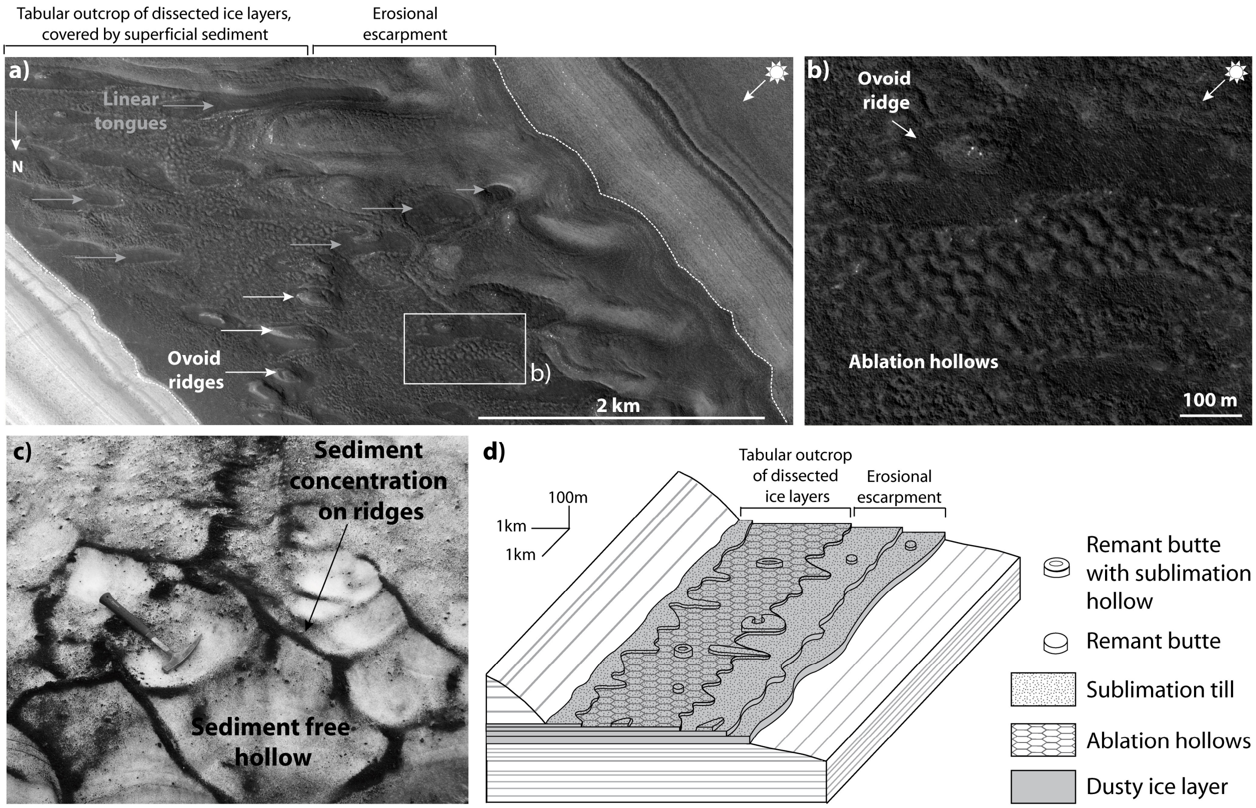
Tabular outcrop of dissected ice layers, covered by superficial sediment
Erosional escarpment
a)
Linear tongues
N
Ovoid ridges
b)
2 km
b)
Ovoid ridge
Ablation hollows
100 m
c)
Sediment concentration on ridges
Sediment free hollow
d)
Tabular outcrop of dissected ice layers
Erosional escarpment
100m
1km
1km
Remant butte with sublimation hollow
Remant butte
Sublimation till
Ablation hollows
Dusty ice layer

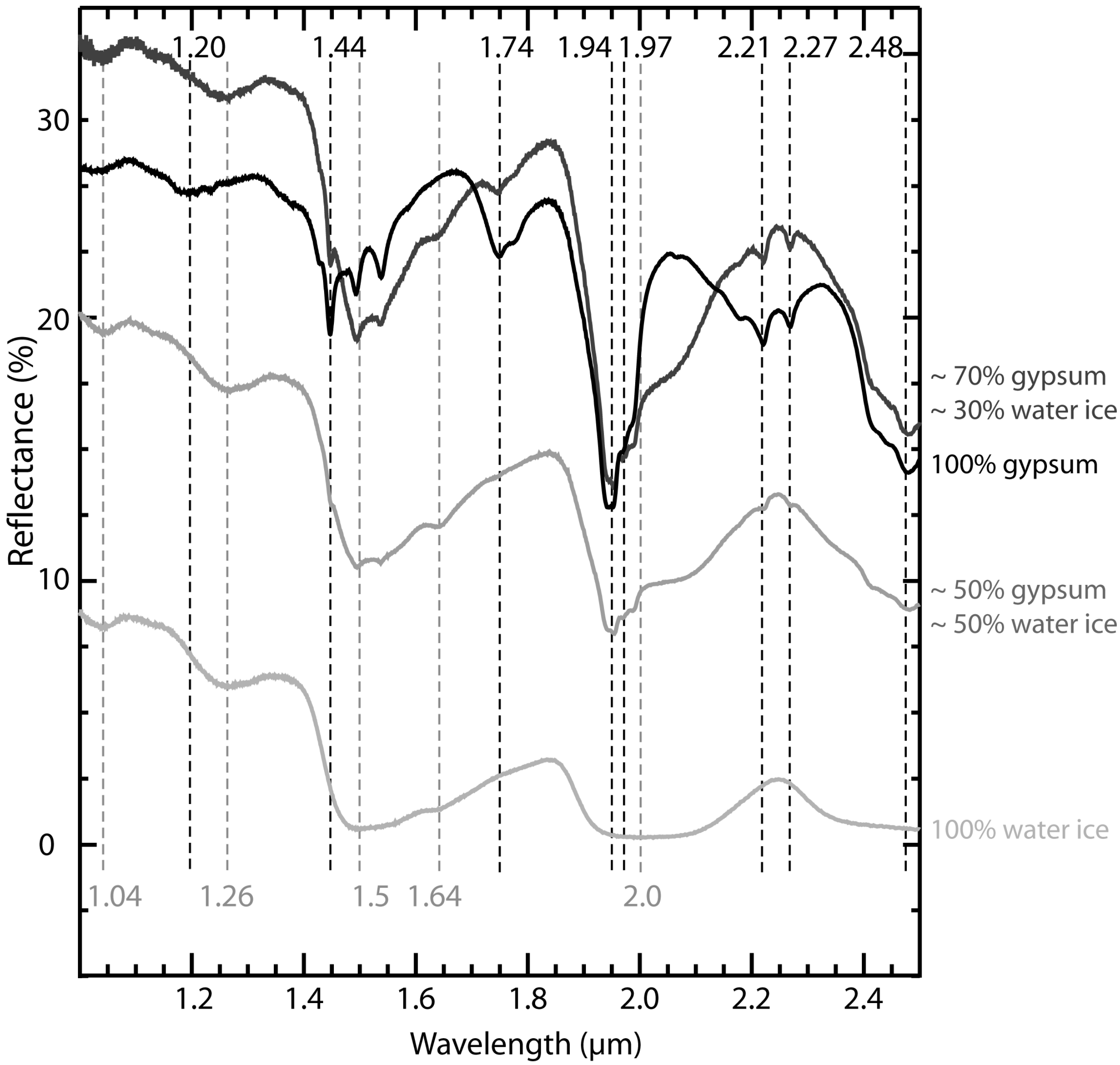
1.20
1.44
1.74
1.94
1.97
2.21
2.27
2.48
30
20
10
0
Reflectance (%)
~ 70% gypsum
~ 30% water ice
100% gypsum
~ 50% gypsum
~ 50% water ice
100% water ice
1.04
1.26
1.5
1.64
2.0
1.2
1.4
1.6
1.8
2.0
2.2
2.4
Wavelength (µm)

1136

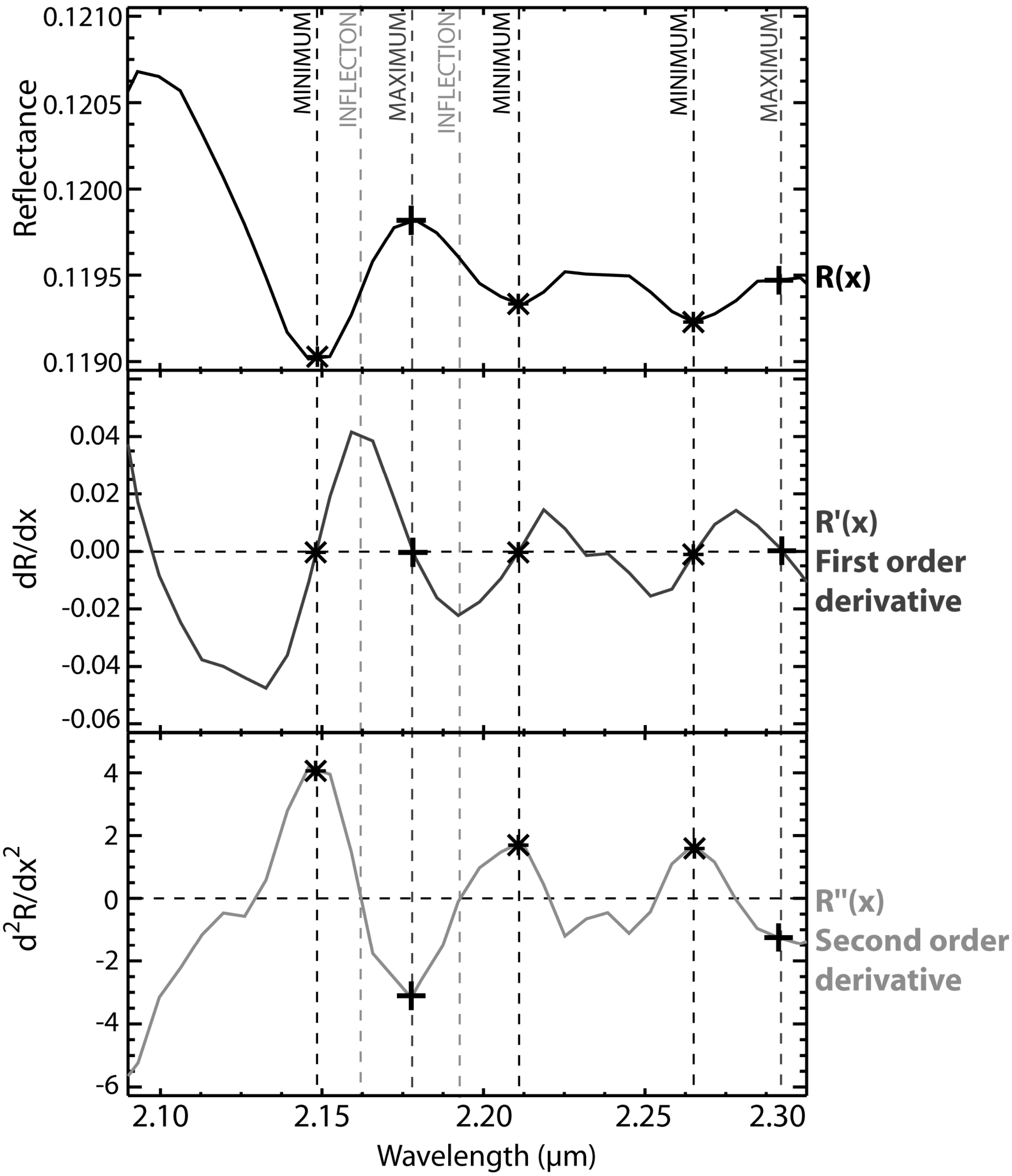
MINIMUM
INFLECTON
MAXIMUM
INFLECTION
MINIMUM
MINIMUM
MAXIMUM
Reflectance
0.1210
0.1205
0.1200
0.1195
0.1190
R(x)
dR/dx
0.04
0.02
0.00
-0.02
-0.04
-0.06
R'(x)
First order derivative
d2R/dx2
4
2
0
-2
-4
-6
R''(x)
Second order derivative
2.10
2.15
2.20
2.25
2.30
Wavelength (µm)

1137

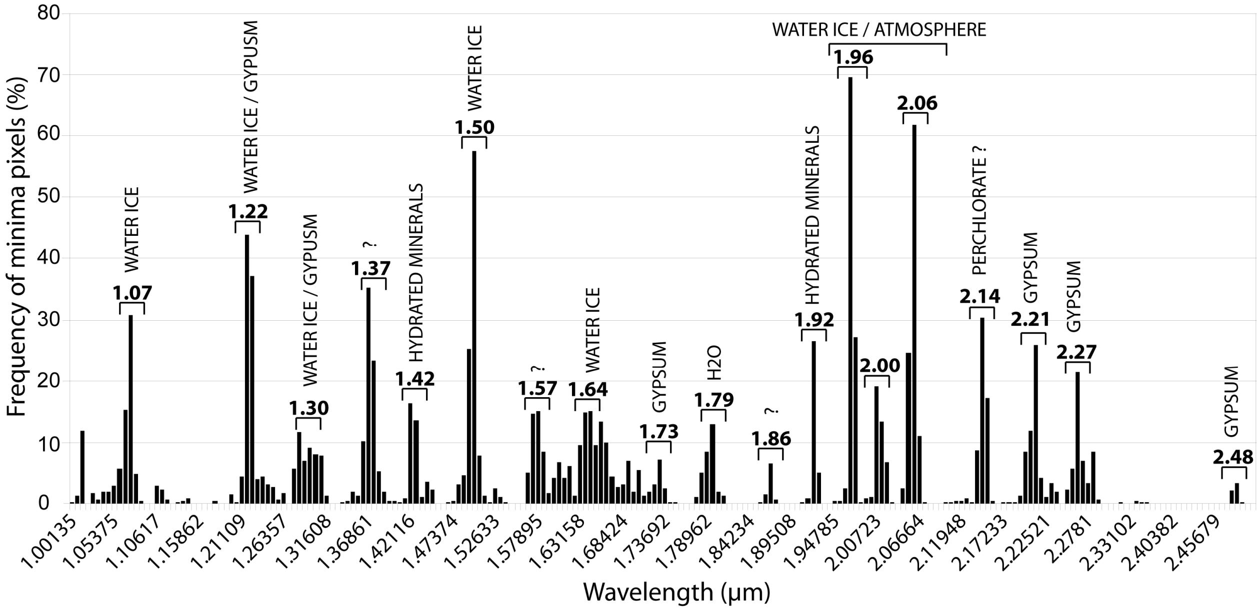

Frequency of minima pixels (%)
Wavelength (µm)
WATER ICE
1.07
WATER ICE / GYPUSM
1.22
WATER ICE / GYPUSM
1.30
?
1.37
HYDRATED MINERALS
1.42
WATER ICE
1.50
?
1.57
WATER ICE
1.64
GYPSUM
1.73
H2O
1.79
?
1.86
HYDRATED MINERALS
1.92
WATER ICE / ATMOSPHERE
1.96
2.00
2.06
PERCHLORATE ?
2.14
GYPSUM
2.21
GYPSUM
2.27
GYPSUM
2.48
0
10
20
30
40
50
60
70
80
1.00135
1.05375
1.10617
1.15862
1.21109
1.26357
1.31608
1.36861
1.42116
1.47374
1.52633
1.57895
1.63158
1.68424
1.73692
1.78962
1.84234
1.89508
1.94785
2.00723
2.06664
2.11948
2.17233
2.22521
2.2781
2.33102
2.40382
2.45679

1138

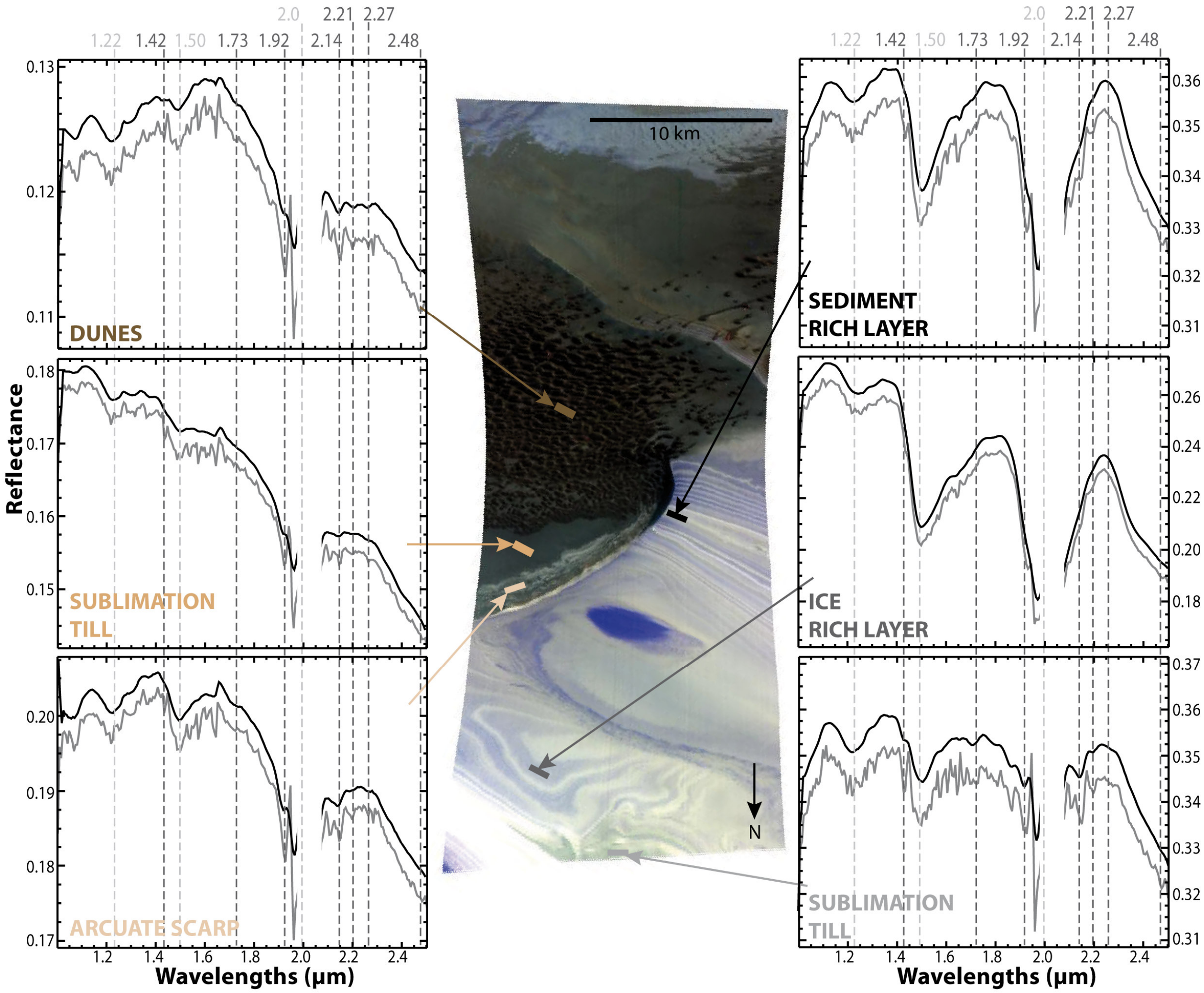

DUNES
SUBLIMATION TILL
ARCUATE SCARP
SEDIMENT RICH LAYER
ICE RICH LAYER
SUBLIMATION TILL
10 km
N
Reflectance
Wavelengths (µm)
1.22 1.42 1.50 1.73 1.92 2.0 2.14 2.21 2.27 2.48

1139

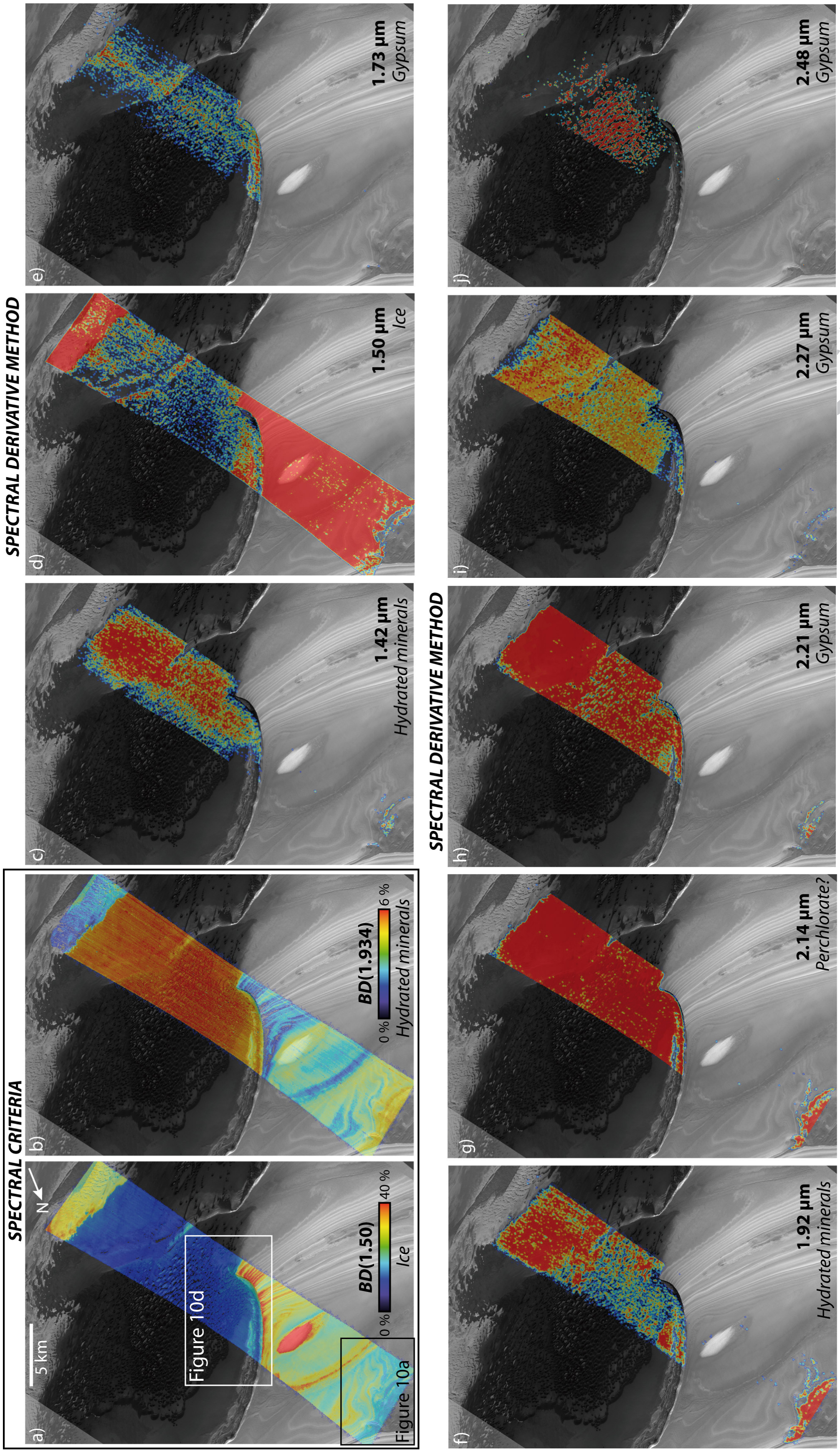
SPECTRAL CRITERIA
a)
N
5 km
Figure 10d
Figure 10a
BD(1.50)
0 %
40 %
Ice
b)
BD(1.934)
0 %
6 %
Hydrated minerals
c)
1.42 µm
Hydrated minerals
SPECTRAL DERIVATIVE METHOD
d)
1.50 µm
Ice
e)
1.73 µm
Gypsum
f)
1.92 µm
Hydrated minerals
g)
2.14 µm
Perchlorate?
SPECTRAL DERIVATIVE METHOD
h)
2.21 µm
Gypsum
i)
2.27 µm
Gypsum
j)
2.48 µm
Gypsum

1141

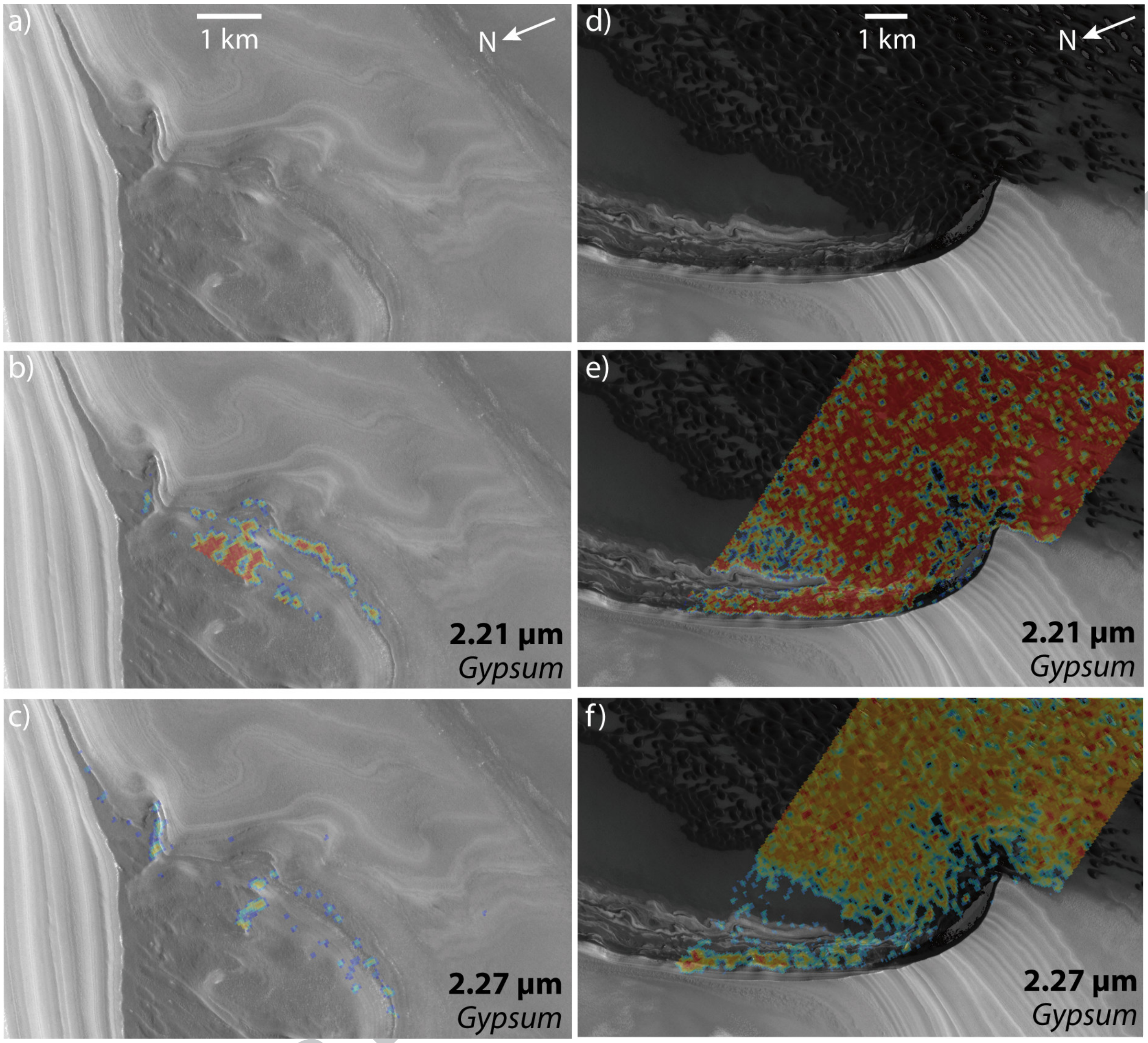
a)
1 km
N
d)
1 km
N
b)
2.21 µm
Gypsum
e)
2.21 µm
Gypsum
c)
2.27 µm
Gypsum
f)
2.27 µm
Gypsum

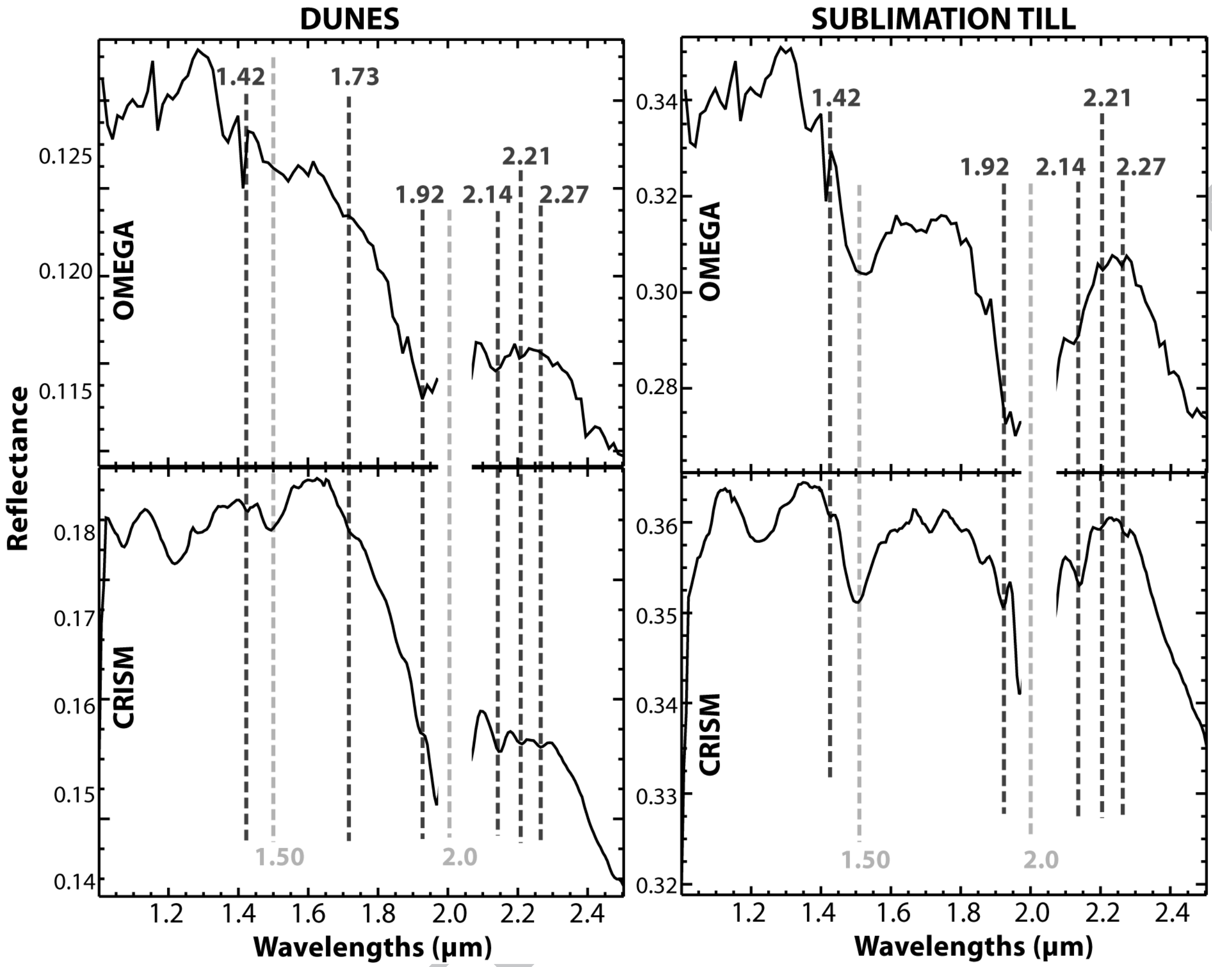
DUNES
SUBLIMATION TILL
Reflectance
OMEGA
CRISM
1.42
1.73
1.92
2.14
2.21
2.27
1.50
2.0
0.125
0.120
0.115
0.18
0.17
0.16
0.15
0.14
0.34
0.32
0.30
0.28
0.36
0.35
0.34
0.33
0.32
1.2
1.4
1.6
1.8
2.0
2.2
2.4
Wavelengths (μm)

1142

1143 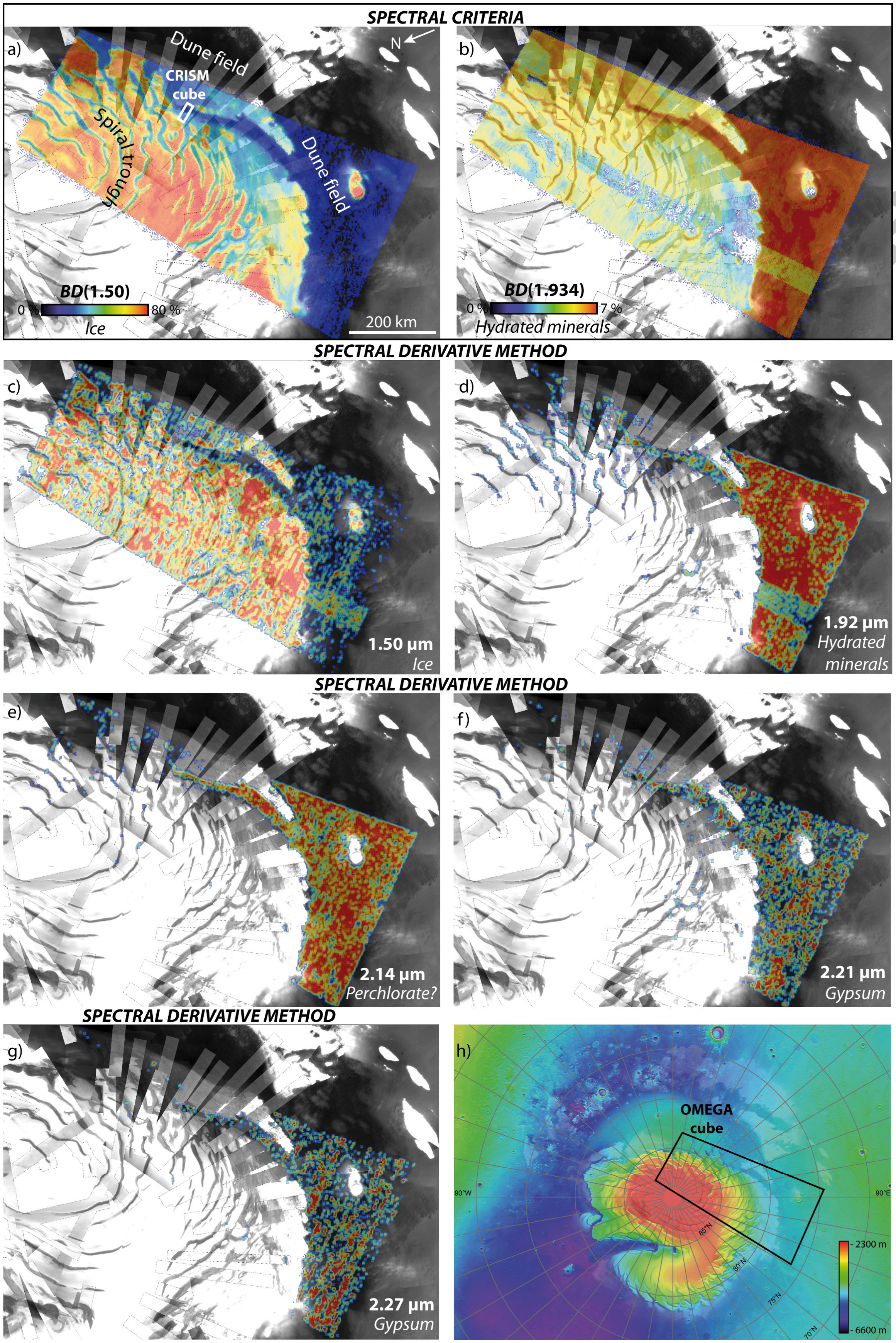
SPECTRAL CRITERIA
a)
Dune field
N
CRISM cube
Spiral trough
Dune field
BD(1.50)
0 %
80 %
Ice
200 km
b)
BD(1.934)
0 %
7 %
Hydrated minerals
SPECTRAL DERIVATIVE METHOD
c)
1.50 µm
Ice
d)
1.92 µm
Hydrated minerals
SPECTRAL DERIVATIVE METHOD
e)
2.14 µm
Perchlorate?
f)
2.21 µm
Gypsum
SPECTRAL DERIVATIVE METHOD
g)
2.27 µm
Gypsum
h)
OMEGA cube
90°W
90°E
85°N
80°N
75°N
70°N
- 2300 m
- 6600 m

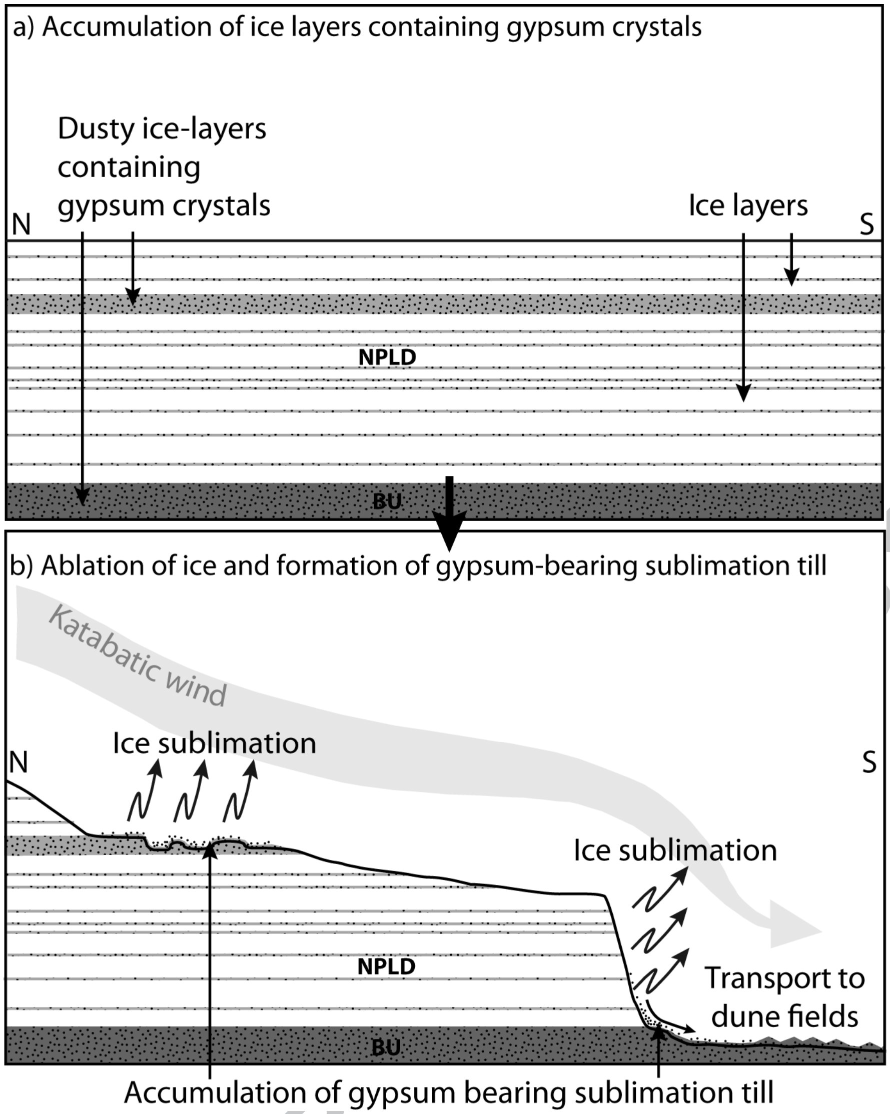
a) Accumulation of ice layers containing gypsum crystals
Dusty ice-layers containing gypsum crystals
Ice layers
N
S
NPLD
BU
b) Ablation of ice and formation of gypsum-bearing sublimation till
Katabatic wind
Ice sublimation
N
S
Ice sublimation
NPLD
Transport to dune fields
BU
Accumulation of gypsum bearing sublimation till

1144